Chapter 1

Generalized Ensemble Computer Simulations of Macromolecules

Wolfhard Janke

Institut für Theoretische Physik, Universität Leipzig,
Postfach 100 920, 04009 Leipzig, Germany,
wolfhard.janke@itp.uni-leipzig.de

In the last two decades computer simulations in generalized ensembles based on Markov chain Monte Carlo sampling such as the multicanonical, Wang-Landau, and parallel tempering (or replica exchange) methods have emerged as a strong numerical tool for investigations of the statistical physics of macromolecular systems. Many studies have focused on coarse-grained models of polymers on the lattice and in the continuum. Phase diagrams of polymer chains in bulk and in interaction with surfaces were extensively studied. Also, the aggregation behavior in solution has been investigated.

In this chapter, first the theoretical background for these simulations will be described, the employed algorithms explained and their performance assessed. Implementations of these algorithms on parallel computers are also briefly discussed. As an illustration of these concepts, an overview of polymer systems investigated with multicanonical and parallel tempering simulations will be given, focusing on our own recent studies of coarse-grained models.

Contents

1. Introduction

Computer simulation studies have become an increasingly important numerical tool for the study and understanding of macromolecular systems. Depending on the application at hand and the degree of chemically realistic modeling of the macromolecular constituents, the results of simulations may be directly compared with experimental data or used to judge the reliability of approximations that are unavoidable in the theory of mesoscopic systems. It is fair to say that the predictive power of state-of-the-art computer simulations has reached a degree where they can be considered as the third cornerstone of modern polymer science beyond experiments and analytical theory.

Two main approaches can be distinguished: Molecular dynamics (MD) and Monte Carlo (MC) simulations. Molecular dynamics simulations[1–3] are based on numerical integration of Newton's nonlinear, coupled equations of motion of the system. In the original formulation, they deliver information on its thermodynamics, structure and dynamics in the microcanonical (NVE) ensemble. Later, by supplementing the method with so-called thermostats, also the canonical (NVT) ensemble became accessible. Monte Carlo methods,[2,4–7] on the other hand, rely from the beginning on the stochastic ensemble formulation of statistical physics. While most studies consider the canonical ensemble, the method can be readily adapted to other ensembles (NVE, NPT, ...) as well. Monte Carlo simulations are mainly geared towards providing thermodynamic and structural information but with some care can be also used to study relaxation behavior.

The great success of computer simulations depends in part on the constant improvements of the computer hardware, but in particular Monte Carlo simulations have even profited more from considerable methodological improvements. An important class of such improvements are the very successful generalized-ensemble Monte Carlo techniques which are in the focus of the present lecture notes.

The rest of this Chapter is organized as follows. In Ssection 2 a brief introduction into generalized ensemble Monte Carlo computer simulations is given, focusing on the multicanonical method and parallel tempering. Section 3 is devoted to applications of such Monte Carlo simulations to macromolecular systems. First, for isolated polymer chains, the employed models and commonly used move sets for the Monte Carlo updates are explained. Then the most important observables are described which are used to map out the phase structure of flexible and semiflexible polymers. The latter

case features a much richer conformation morphology, including phases with stable knots which are described in some detail. The following Subsection 3.2 gives an overview on polymer adsorption studies for various geometries, including the chemically realistic case of Poly(3-hexylthiophene-2,5-diyl) (P3HT) macromolecules in contact with a clean gold substrate under ultra-high vacuum conditions, for which the results of our computer simulations are compared with recent experimental data. Next, polymer aggregation is discussed in Subsection 3.3 first for heteropolymers in the frame of the hydrophobic-polar (HP) lattice model and then for continuum formulations of mesoscopic systems of flexible and semiflexible polymers. For the case of flexible polymers, an analogy to particle condensation will be drawn as far as possible. Finally, in Section 4 a brief summary of the presented results is given.

2. Generalized Ensemble Computer Simulations

Generalized ensemble simulation techniques rely on standard importance sampling Monte Carlo methods which are described in many textbooks and reviews.[2,4–7] For later reference when discussing the more refined techniques, it is still helpful to start here at least with a brief summary of the essential features of the most prominent representative, Monte Carlo simulations in the canonical ensemble, which is defined by fixing the macroscopic variables particle number, N, volume, V, and temperature, T. According to statistical physics, every conformation or microstate, x, occurs with the probability

$$p_{\rm eq}(x) = \frac{1}{Z(N,V,T)} {\rm e}^{-\beta E_p(x)} \ , \tag{1}$$

where $\beta = 1/k_{\rm B}T$ is the inverse temperature and $E_p(x)$ the potential energy of the system. The normalization factor is the canonical partition function

$$Z(N,V,T) = \int_{\mathcal{X}} \mathcal{D}x {\rm e}^{-\beta E_p(x)} = \int dE_p \, g(N,V,E_p) {\rm e}^{-\beta E_p} \ , \tag{2}$$

where $\mathcal{X}$ denotes the conformation space of the system and $g(N,V,E_p)$ is the conformational density of states, which is closely related to the microcanonical partition function $\Gamma(N,V,E)$. Here $E = E_k + E_p$ is the *total* energy. One crucial point is that in (2) we have implicitly assumed that all momentum degrees of freedom p have already been integrated out, which is straightforward as long as the potential energy E_p depends only on x

and the kinetic energy $E_k \propto p^2$ is of the generic form, leading to a decoupled multi-dimensional Gaussian integral. The expectation value of an observable $A(x)$ is given by

$$\langle A \rangle = \int_{\mathcal{X}} \mathcal{D}x A(x) p_{\rm eq}(x) \; . \tag{3}$$

This is a multi-dimensional integral which can be estimated by sampling a rather small number of well selected points through a Markov chain defined by the process

$$p(x',n+1) = p(x',n) + \int_{\mathcal{X}} \mathcal{D}x W(x'|x) p(x,n) - \int_{\mathcal{X}} \mathcal{D}x W(x|x') p(x',n) \; , \tag{4}$$

where $W(x'|x)$ is the transition density for going from state x at discrete time n to x' at time $n+1$. The mathematical theory of Markov chains shows under which conditions the equilibrium distribution is approached. In physics language, the detailed balance condition is the most important one,

$$\frac{W(x'|x)}{W(x|x')} = \frac{p_{\rm eq}(x')}{p_{\rm eq}(x)} = {\rm e}^{-\beta[E_p(x')-E_p(x)]} \; . \tag{5}$$

Detailed balance is satisfied in, e.g., the Metropolis update algorithm where an update from an old conformation x to a new conformation x' is proposed and accepted with probability

$$p_{\rm acc}(x \to x') = \min(1, {\rm e}^{-\beta[E_p(x')-E_p(x)]}) \; . \tag{6}$$

This is a basic ingredient of any generalized-ensemble algorithm, too. Since in most of our recent investigations of polymer systems we employed multicanonical simulations[8–10] and the parallel tempering method,[11] the main focus of these lecture notes will be on these two representatives of generalized-ensemble algorithms. Their properties have been described in many reviews mainly in the context of spin models.[6,12–17] For two recent reviews with emphasis on macromolecular systems, see Refs. 18 and 19. In the former review also the related Wang-Landau method[20–25] and the more recent stochastic approximation Monte Carlo (SAMC) approach,[26–31] rooted in mathematical statistics, are discussed in detail.

2.1. *Multicanonical method*

The idea of multicanonical ("muca") Monte Carlo methods dates back to the work of Berg and Neuhaus[8,9] in 1991/92. In two seminal papers they proposed a novel simulation approach for overcoming the exponential

(sometimes called "super-critical") slowing down of Monte Carlo simulations at first-order phase transitions in the canonical ensemble. Consider a temperature-driven first-order phase transition where in a finite system the phase coexistence is reflected by a double peak of the energy[a] distribution $P_{\mathrm{can},\beta}(E)$, with the minimum in between governed by the interface tension σ_{od} between the coexisting ordered and disordered phases: $P_{\min}/P_{\max} \propto \exp(-2\sigma_{od}L^{d-1})$. Here L is the linear size of a d-dimensional cubic system and periodic boundary conditions are assumed, explaining the factor 2 in the exponent. Due to this exponential suppression with increasing system size, it is very unlikely to transit in a canonical simulation from one phase to the other and hence it is very time consuming to generate accurate equilibrium results.

By "filling" this rare-event region with an artificial weight factor $W(E)$ (to be determined below), the multicanonical method may be viewed as a specific realization of non-Boltzmann sampling which has been known since long as a legitimate alternative to more standard Monte Carlo approaches.[32] In this interpretation, the multicanonical method appears as a non-standard reweighting approach,[10] a view which in most cases simplifies the actual implementation and paves the way to multidimensional generalizations. Alternatively, the method may be interpreted as a suitable (dynamic) combination of canonical statistics over an extended temperature or energy range in a *single* simulation run, instead of patching *many* independent canonical simulations at different temperatures as in (static) reweighting procedures such as the weighted histogram analysis method (WHAM).[33–35] The latter view is stressed in the original papers by Berg and Neuhaus[8,9] and suggests the name "*multi*-canonical".

It should be noted that the practical significance of non-Boltzmann sampling has, in fact, already been demonstrated much earlier by Torrie and Valleau[36] with the "umbrella sampling" method. Most of these early applications aimed at reliable computations of free-energy differences which can be obtained by canonical Boltzmann sampling only indirectly via so-called thermodynamic integration. Later the attention slowly shifted to problems with rare-event sampling and quasi-ergodicity,[37] but it took many years before the development of the multicanonical scheme turned non-Boltzmann sampling into a widely appreciated practical tool in computer simulation studies. Once the feasibility of such generalized ensemble approach was re-

[a]Here and in the following we simplify the notation and adopt the usual convention of using the symbol E for the *potential* energy as long as kinetic energies are not explicitly involved.

alized, it was for instance readily introduced into protein folding studies[17,38] and many related methods were developed.

The multicanonical method is a two-step process, where one first iteratively improves guesses of the a priori unknown weight function $W(E)$ for, e.g., polymer conformations (microstates) x with system energy $E(x)$, which replaces the usual Boltzmann weight $\mathrm{e}^{-\beta E}$ in the canonical partition function (2):

$$\begin{aligned} Z(T) &= \sum_x \mathrm{e}^{-\beta E(x)} = \sum_E g(E)\mathrm{e}^{-\beta E} \\ \to Z_{\mathrm{muca}} &= \sum_x W\left(E\left(x\right)\right) = \sum_E g(E)W(E)\ . \end{aligned} \tag{7}$$

Here and in the following we omit the arguments N, V of the canonical partition function and the (conformational) density of states. Correspondingly, the acceptance probability (6) of traditional Metropolis Monte Carlo simulations is modified to

$$\begin{aligned} p_{\mathrm{acc}}(x \to x') &= \min(1, \mathrm{e}^{-\beta(E'-E)}) \\ &\to \min(1, \frac{W(E')}{W(E)})\ , \end{aligned} \tag{8}$$

where $E \equiv E_{\mathrm{old}}$ is the current or "old" energy of the conformation x and $E' \equiv E_{\mathrm{new}}$ the "new" energy of a proposed updated conformation x'. As in Metropolis simulations, the update proposals for going from a conformation x to a conformation x' may be local (such as end rotation, bend, or crankshaft moves for polymers) or non-local (such as spherical rotation or pivot moves).

The key of the multicanonical method lies in the first step where the weight $W(E)$ is usually adjusted in such a way that the transition probabilities between configurations with different energies become roughly constant, giving an approximately flat energy histogram

$$H(E) \propto P_{\mathrm{muca}}(E) = g(E)W(E) \approx \mathrm{const.} \tag{9}$$

If this can be achieved, the simulation thus performs approximately a random walk through energy space. The formal solution of (9) is $W(E) = g^{-1}(E)$. However, since the density of states $g(E)$ is usually not known beforehand one has to proceed by a weight iteration which is initialized by setting $W(E) = W^{(0)}(E) \equiv 1$. One thus starts with a standard canonical simulation at $\beta = 0$ which yields $H^{(0)}(E) \propto P_{\mathrm{can},\beta=0}(E)$. This current multicanonical histogram is then used to determine the next guess for the weights, the simplest update is to calculate $W^{(1)}(E) = W^{(0)}(E)/H^{(0)}(E)$.

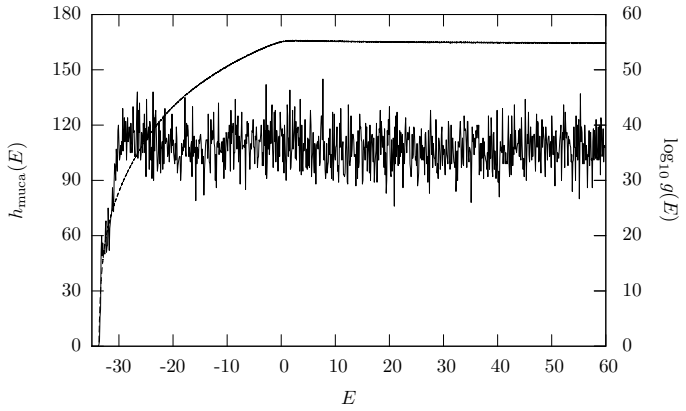

Fig. 1. The almost horizontal line fluctuating between $90 - 120$ counts per energy bin shows the flat multicanonical energy histogram $h_{\rm muca}(E)$ and the smooth curve spanning about 50 orders of magnitude depicts the resulting density of states $g(E)$. The data are obtained from a multicanonical simulation of an AB heteropolymer with 20 monomers forming the sequence $BA_6BA_4BA_2BA_2B_2$ (taken from Ref. 39).

The following run is performed with $W^{(1)}(E)$ inserted in (7) and (8), which gives the energy histogram $H^{(1)}(E)$ and an improved estimate of the weight function, $W^{(2)}(E) = W^{(1)}(E)/H^{(1)}(E)$. This iterative procedure can be continued,

$$W^{(n+1)}(E) = W^{(n)}(E)/H^{(n)}(E) \; , \tag{10}$$

until the multicanonical histogram $H^{(n)}(E)$ is judged to be "flat" enough. From (10) it is obvious that once $H^{(n)}(E) \approx$ const., $W^{(n+1)}(E) \propto W^{(n)}(E) \propto g^{-1}(E)$ is at a fixed point of the iteration and will not change anymore.

An example for an AB heteropolymer chain[39] is shown in Fig. 1. Here the density of states $g(E)$ varies over about 50 orders of magnitude. This sounds already like a lot, but once the multicanonical iteration is set up, this can be driven even much further[40,41] as is demonstrated in Fig. 2, where the density of states for a homopolymer with 309 monomers covers more than 3000 orders of magnitude.

An important parameter of this procedure is the simulation length $N^{(n)}$ in the nth iteration step. If this is too small, the resulting multicanonical histogram is very noisy, which enters directly in the generalized Boltzmann probabilities of the next iteration step. On the other hand, in order to optimize the total time needed to construct the final multicanonical weight,

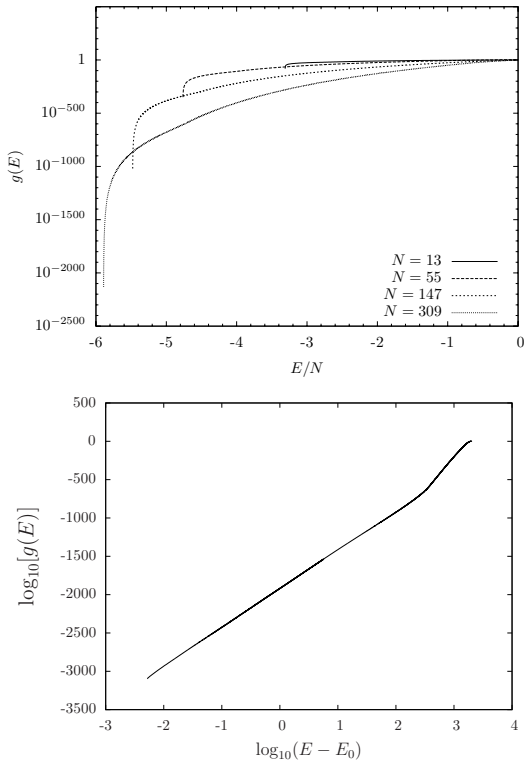

Fig. 2. (top) Density of states of bead-spring homopolymers consisting of N monomers connected by FENE springs and interacting through a (truncated) Lennard-Jones potential, forming for these "magic" N values complete icosahedra (from Ref. 40). (bottom) Log-log representation of the density of states for $N = 309$ ($E_0 = -1820.684$), covering more then 3000 orders of magnitude (from Ref. 41).

$N^{(n)}$ should also not be chosen too large. Since here also autocorrelation times (in the intermediate multicanonical simulations during the iteration) play an important role, it is difficult to give an a priori estimate for the optimal values of $N^{(n)}$ (which, in fact, may vary with the iteration level n).

A more sophisticated recursion, in which the new weight factor is computed from *all* available data accumulated so far, reduces the dependency on $N^{(n)}$ significantly and as a consequence is much more robust. Recalling that in the acceptance probability (8) only weight ratios enter, it is useful to define $R(E) = W(E + \Delta E)/W(E)$ with some ΔE. The accumulative weight iteration then works as follows:

1. Perform a simulation with $R^{(n)}(E)$ to obtain the histogram $H^{(n)}(E)$, taking $N^{(n)}$ energy measurements.
2. Compute the statistical weight of the nth run:
$$p(E) = H^{(n)}(E)H^{(n)}(E+\Delta E)/[H^{(n)}(E)+H^{(n)}(E+\Delta E)] \; . \quad (11)$$
3. Accumulate statistics:
$$p^{(n+1)}(E) = p^{(n)}(E) + p(E) \; , \quad (12)$$
$$\kappa(E) = p(E)/p^{(n+1)}(E) \; . \quad (13)$$
4. Update weight ratios:
$$R^{(n+1)}(E) = R^{(n)}(E) \left[H^{(n)}(E)/H^{(n)}(E+\Delta E)\right]^{\kappa(E)} \; . \quad (14)$$
Goto step 1.

The recursion is initialized with $p^{(0)}(E) = 0$. Due to the accumulated statistics, this procedure is rather insensitive to the length $N^{(n)}$ of the nth run in step 1. The idea behind (11) is that the a priori error estimate for a histogram $H(E)$ (normalized to total counts) is given by $\sqrt{H(E)}$. The rest is basically just error propagation. Of course, to arrive at handy and easy-to-use formulas some approximations are necessary, such as neglecting autocorrelation times, cross-correlations in histograms etc., but apart from that the accumulative recursion has a firm theoretical basis.

Another option to tune the performance of the weight iteration for the problem at hand is an appropriate choice of the energy range, in which the "flattening" of the multicanonical distribution is started. For instance, for a temperature driven first-order phase transition it may be useful to place this range in the regime between the two peaks of $P_{\mathrm{can},\beta}(E)$ associated with the disordered and ordered phases. This can be simply achieved by setting initially $W^{(0)}(E) \equiv e^{-\beta_0 E}$ (instead of $\equiv 1$) for a suitably chosen β_0. This corresponds to a canonical simulation at $\beta = \beta_0$ in the 0th iteration step, resulting in $H^{(0)}(E) \propto P_{\mathrm{can},\beta_0}(E)$ which covers the desired energy range around $\langle E\rangle(\beta_0)$. The remaining iteration then proceeds as before. Note that for some problems it may be in fact sufficient to stop the iteration once the region between the two canonical peaks is flat.

Finally it should be stressed that also when employing flat-histogram ideas the choice of update proposals can play a crucial role for the success of polymer simulations.[41] Moreover, it turned out to be very useful to allow the range of the proposed update moves to become energy dependent (at high energies corresponding to high temperatures, large moves will be

accepted, whereas at low energies corresponding to low temperatures, only small moves have a reasonable acceptance probability). Of course, a priori this energy dependence causes violations of detailed balance. This can be regained, however, by introducing suitable bias factors in a Metropolis-Hastings scheme.[41]

After having determined an accurate multicanonical weight $W(E)$, the second step is the actual production run, which works with *fixed* weights. By this one assures that detailed balance is implemented in the same way as in the standard Metropolis Markov chain procedure and any statistical quantity O can be "measured" multicanonically according to

$$\langle O\rangle_{\rm muca} = \sum_x O(x)W(E(x))/Z_{\rm muca}\ . \tag{15}$$

The usually desired canonical statistics can be obtained by reweighting the multicanonical distribution back to the canonical one, e.g., canonical expectation values (3) are computed as

$$\langle O\rangle(\beta) = \langle O{\rm e}^{-\beta E}W(E)^{-1}\rangle_{\rm muca}/\langle {\rm e}^{-\beta E}W(E)^{-1}\rangle_{\rm muca}\ . \tag{16}$$

Note that this representation is exact for any choice of $W(E)$. As usual, in a simulation run with N measurements, the expectation values are replaced by mean values (their "estimators"), e.g.,

$$\langle O\rangle(\beta) \approx \sum_{i=1}^{N} O_i{\rm e}^{-\beta E_i}W(E_i)^{-1}/\sum_{i=1}^{N}{\rm e}^{-\beta E_i}W(E_i)^{-1}\ . \tag{17}$$

Of course, replacing the ratio of expectation values on the right-hand side of (16) by averages is in principle prone to bias effects, but here strong cross-correlations act positively and keep this potential problem small.

At times where the computer performance increases mainly in terms of parallel processing on multi-core architectures, it is crucial to parallelize the applied algorithm. For an in-depth discussion of parallel computing, see Chapter XX of this book by Martin Weigel. With this in mind, we have recently developed a parallelized variant of the multicanonical method.[42] The parallelization relies on independent equilibrium simulations with many "walkers" (or "workers"), which only communicate when the multicanonical weight function is updated. This structure is also perfectly suited for implementation on graphics processing units (GPUs).[43] In this way, the independent Markov chains efficiently sample the temporary distributions, allowing for good estimations of consecutive weight functions. For similar approaches see Refs. 44,45.

Overall, the parallelization was shown to scale quite well in applications to generic spin models and coarse-grained polymers.[42,46,47] In all cases, a close to linear scaling was observed with slope one for up to 128 cores used. This means that doubling the number of involved processors would reduce the required wall-clock time by a factor of two. Our method is a straightforward and simple implementation, especially if wrapped around an existing multicanonical simulation code. Therefore the parallelization can be easily generalized also to other flat-histogram simulations, e.g., multimagnetic simulations where the magnetization[48,49] or any other order-parameter[50,51] distribution is flattened. It should be emphasized that no greater adjustment to the usual implementation is necessary and that additional modifications may be carried along. This allows a straightforward application of this parallelization to a broad class of complex systems such as (bio) polymers and (spin) glasses.

2.2. *Parallel tempering*

In the parallel tempering approach[11] (also often referred to as replica exchange) one follows a different strategy and performs simulations of m replicas of the system at different temperatures $T_\mu = 1/\beta_\mu$. Every now and then the conformations x_μ and x_ν of two (usually neighboring) replicas μ and ν are proposed to be exchanged. Detailed balance is ensured if such exchanges are accepted with probability

$$p_{\text{acc}}\left(x_\mu \leftrightarrow x_\nu\right) = \min\left(1, \exp\left(\Delta\beta\Delta E\right)\right) \ , \tag{18}$$

where we used the abbreviations $E_\mu = E(x_\mu)$, $E_\nu = E(x_\nu)$, and $\Delta X = X_\mu - X_\nu$.

The efficiency of parallel tempering is mainly governed by three control parameters, the spacings of the simulation temperatures T_μ, the temperature-dependent run times for each replica, and the frequency of the attempted conformation exchanges. As the most crucial condition, in general one has to make sure that by adapting the temperature spacings the energy histograms at neighboring temperatures sufficiently overlap. Usually this guarantees already a reasonably well performing simulation. More elaborate optimization strategies have been discussed, e.g., in Refs. 52–55.

3. Applications to Marcomolecular Systems

3.1. *Isolated polymer chains*

It is well know that the structural motifs of isolated polymer chains depend strongly on external parameters such as temperature or salt concentration. Also the internal parameter of bending stiffness, governing the interpolation between *flexible* and *semiflexible* polymers, plays a crucial role.

3.1.1. *Models*

The bonds connecting the monomers of the polymer chain are either modeled in bead-*stick* models by stiff bonds of fixed length r_0 or in bead-*spring* models by some sort of spring. Besides a simple harmonic oscillator potential, one often employs a finitely extensible nonlinear elastic (FENE) potential, which for small elongations is essentially a harmonic potential with spring constant K around the bond length r_0, but for larger elongations becomes steeper and eventually diverges at a maximal extension R:

$$V_{\rm FENE}(r) = -\frac{K}{2} R^2 \ln\left(1 - [(r - r_0)/R]^2\right) \ , \tag{19}$$

where we follow the conventions used in Refs. 40,56.

The interaction among the monomers is usually modeled by a distance-dependent 12–6 Lennard-Jones (LJ) potential,

$$E_{\rm LJ} = 4\epsilon_{\rm LJ} \sum_{i=1}^{N-2} \sum_{j=i+2}^{N} \left[\left(\frac{\sigma}{r_{ij}}\right)^{12} - \left(\frac{\sigma}{r_{ij}}\right)^{6} \right] \ , \tag{20}$$

accounting for short-range excluded volume repulsion and long-range interaction of non-bonded monomers at distance $r_{ij} = |\vec{r}_i - \vec{r}_j|$. Each summand in (20) is minimized for $r_{ij} = 2^{1/6}\sigma$ where it contributes $-\epsilon_{\rm LJ}$ to $E_{\rm LJ}$. In the simulations one usually sets $\epsilon_{\rm LJ}$ to unity, fixing the energy scale.

The bending stiffness of a *semiflexible* polymer is introduced via its discretized curvature which leads to the worm-like chain (WLC)[57,58] inspired bending potential,

$$V_{\rm bend}(\theta_i) = \kappa(1 - \cos\theta_i) \ , \tag{21}$$

where θ_i is the angle between consecutive bonds and κ is a tunable bending-stiffness parameter which, in the pure WLC with $\epsilon_{\rm LJ} \equiv 0$ and stiff bonds, is directly related to the persistence length of the polymer chain. This is the prime parameter varied in many studies, allowing to cover the whole class of semiflexible polymers from flexible ($\kappa = 0$) to rather rigid (κ large) in a systematic way.

3.1.2. *Move sets for polymer updates*

In general the choice of the update move sets is very important for efficient simulations of macromolecular systems. This is well known for ordinary Metropolis-like Monte Carlo simulations, where the autocorrelation times depend quite sensitively on them,[59] but also for the performance of multicanonical and parallel tempering methods they play an important role. Here only a few of the most popular and successful ones are briefly described. For a more comprehensive overview with references to the original literature, see Ref. 60.

Crankshaft update: The crankshaft update method is local in the sense that only the coordinates of a single monomer are changed. The crankshaft move picks a random monomer. The two neighbouring and bonded monomers build an axis about which it is then rotated by an angle in the interval $[0, \omega)$, with $\omega \leq 2\pi$, cf. Fig. 3 (right). Note that the two end points can never be picked, since they do not have two bonding neighbors. The crankshaft move is hence not ergodic, which can be fixed, however, by combining it with any of the following non-local update methods.

Pivot update: One of the most used methods for updating polymer conformations is the pivot move.[61,62] Here one chooses randomly one of the monomers and lays an axis with random direction through its center. The whole end tail of the polymer is then rotated about this axis by a randomly chosen angle $\Delta\varphi \in [0, 2\pi)$. For a sketch, see Fig. 3 (center). This means that normally all but one pair of bonds keep the same angle relations. It is possible that the orientation of the axis is the same as one of the two bonds at the chosen monomer. In that case the end tail is rather only twisted in a torsion-like movement and it is possible that none of the bond angles changes. Detailed balance can be shown to be satisfied.

Spherical update: The spherical update method[63] is similar to the pivot move. Here one of the $N-1$ bonds is picked randomly with equal probability. This k-th bond is rotated and all following bonds $> k$ (and monomers) are translated. The orientation of these following bonds is not changed. This is illustrated in Fig. 3 (left). Due to the self-avoidance of the polymer, the acceptance probabilities should not be too small. This can be achieved by restricting the opening angle to a value $2\Delta\vartheta_{\max}$. Graphically represented this means that the bond can only move on a spherical cap. For

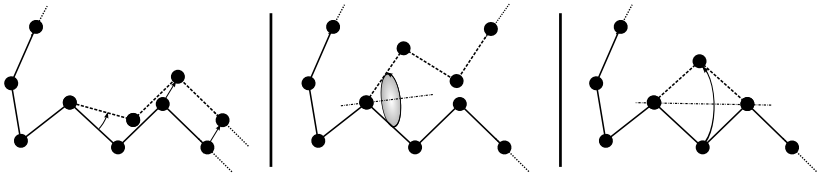

Fig. 3. Illustrations of the spherical (left), pivot (center) and crankshaft (right) update method. The proposed new conformation is drawn with thick dotted lines while the dashed-dotted lines indicate the rotation axis.

this, two angles have to be evaluated: The bonding angle $\Delta\vartheta$ and the rotation angle $\Delta\varphi$, where the correct intervals to choose from are $[0, \Delta\vartheta_{\max})$ and $[0, 2\pi)$, respectively. Because every point on this spherical cap can be reached with equal probability, detailed balance is satisfied.

Double-bridge update: A variant of the well-known (intramolecular) end-bridging move[64] is the so-called double-bridge move. The basic idea of this update method is to exchange two bonds of the polymer. This is done by picking two bonds randomly and removing them. This gives three parts: two dangling ends and one inner part. The latter is shifted such that the monomer of the one dangling end is now connected to the monomer of the inner part, where the other dangling end was connected. The remaining dangling end is now also shifted such that it is connected to the inner monomer, where the first dangling end was connected. This is depicted in Fig. 4. In contrast to the original formulation[64] and to fit our polymer model, the new conformations are chosen such that all bonds are kept at a fixed length.

3.1.3. *Observables*

To obtain as much information as possible about the canonical equilibrium behavior, usually the following quantities O are measured in the simulations. Next to the canonical expectation values $\langle O\rangle$, one also determines the fluctuations around these averages, as given by the temperature derivative $d\langle O\rangle/dT = \left(\langle OE\rangle - \langle O\rangle\langle E\rangle\right)/T^2$. In most simulation studies, generic units ared used in which the Boltzmann constant $k_B = 1$.

For the identification of conformational transitions, the specific heat (per monomer) $C_V(T) = (\langle E^2\rangle - \langle E\rangle^2)/NT^2$ is a useful quantity. Since $\langle E^k\rangle = \sum_E g(E)E^k \exp(-E/T)/\sum_E g(E)\exp(-E/T)$, it can be calcu-

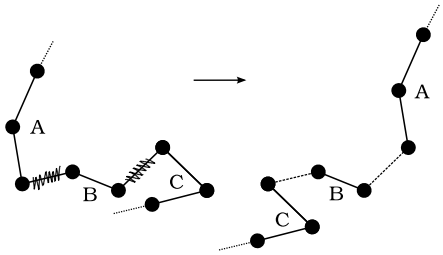

Fig. 4. Illustration of the double-bridge move (keeping monomer distances constant). Two bonds are selected randomly and erased (criss-cross lines). The inner part B is shifted and reconnected to the dangling end C. The dangling end A is then shifted and reconnected to the inner part B. As a result, the dangling ends A and C have swapped their bonds to the inner part B.

lated easily from from the density of states $g(E)$. The density of states in turn can be obtained (up to an unimportant overall normalization constant) by reweighting the multicanonical energy distribution sampled in a multicanonical simulation to the canonical distribution.

Apart from the specific heat, several structural quantities are of interest. In order to check the structural compactness of conformations or to identify the possible dispersion of conformations because of adsorption or aggregation, the radius of gyration of the conformations is calculated. The radius of gyration is a measure for the extension of the polymer and defined by

$$R_{\mathrm{g}}^2 \equiv \sum_{i=1}^{N} (\vec{r}_i - \vec{r}_{\mathrm{cm}})^2 / N = \sum_{i=1}^{N} \sum_{j=1}^{N} (\vec{r}_i - \vec{r}_j)^2 / 2N^2 \;, \tag{22}$$

where $\vec{r}_{\mathrm{cm}} = \sum_{i=1}^{N} \vec{r}_i / N$ is the center-of-mass of the polymer consisting of N monomers (or repeat units). Closely related is the end-to-end distance $R_{\mathrm{e}} = |\vec{r}_N - \vec{r}_1|$, which measures the distance between the last and first monomer.

In our own work we found it useful to calculate also various (invariant) shape descriptors derived from the gyration tensor,[65–69] which is defined as

$$S = \frac{1}{N} \begin{pmatrix} \sum_i (x_i - \overline{x})^2 & \sum_i (x_i - \overline{x})(y_i - \overline{y}) & \sum_i (x_i - \overline{x})(z_i - \overline{z}) \\ \sum_i (y_i - \overline{y})(x_i - \overline{x}) & \sum_i (y_i - \overline{y})^2 & \sum_i (y_i - \overline{y})(z_i - \overline{z}) \\ C \sum_i (z_i - \overline{z})(x_i - \overline{x}) & \sum_i (z_i - \overline{z})(y_i - \overline{y}) & \sum_i (z_i - \overline{z})^2 \end{pmatrix} \;, \tag{23}$$

where $\overline{x} \equiv x_{\rm cm}$ etc. Transformation to the principal axis system diagonalizes S,

$$S = \mathrm{diag}(\lambda_1, \lambda_2, \lambda_3) \;, \tag{24}$$

where it is implicitly assumed that the eigenvalues of S are sorted in descending order, i.e., $\lambda_1 \geq \lambda_2 \geq \lambda_3$. The first invariant of S is just the squared radius of gyration,

$$\mathrm{Tr}\, S = \lambda_1 + \lambda_2 + \lambda_3 = R_{\rm g}^2 \;, \tag{25}$$

which agrees with the explicit definition (22) given above. The second invariant shape descriptor, or relative shape anisotropy, is defined as

$$\kappa^2 \equiv A_3 = \frac{3}{2}\frac{\mathrm{Tr}\hat{S}^2}{(\mathrm{Tr}S)^2} = 1 - 3\frac{\lambda_1\lambda_2 + \lambda_2\lambda_3 + \lambda_3\lambda_1}{(\lambda_1+\lambda_2+\lambda_3)^2} \;, \tag{26}$$

where $\hat{S} = S - \frac{1}{3}(\mathrm{Tr}S)I$ with unit tensor I. It reflects both the symmetry and dimensionality of a polymer conformation. This parameter is limited between the values of 0 and 1. It reaches 1 for an ideal linear chain and drops to zero for highly symmetric conformations. For planar symmetric objects, the relative shape anisotropy converges to the value of $1/4$.[65–70]

The statistical error bars on these observables can be obtained most reliably by Jackknife error analyses.[7,71,72]

3.1.4. *Flexible polymers*

Flexible polymers behave at high temperatures as random coils because conformational entropy dominates the energy reduction of monomer-monomer contact formation. By lowering the temperature, energy minimization becomes more important and in the so-called collapse transition a more compact globular conformation is formed. This is similar to the first-order gas-liquid transition of a particle system. Here, however, the collapse transition is of second order.[73,74] Intuitively this qualitative difference can be traced back to the connectivity constraint of a polymer chain due to which the gain in entropy in the random-coil phase is much less than for particles which can move independently of each other in the gas phase. At a much lower temperature, polymers undergo another first-order-like freezing transition,[40] the analogue of the liquid-solid transition of interacting particles. This scenario is non-trivial, however, as for instance a variation of the short-range attraction range can induce a transition from the random-coil phase directly into this low-temperature frozen state.[75–79] Similarly, a modification of the bond-interaction range can alter the second-order collapse transition into a first-order condensation transition of coupled monomers.[80]

There has been an interesting discussion in the literature about the scaling behavior of the collapse transition temperature $T_\theta(N)$ of a single flexible homopolymer as a function of polymerization, i.e., polymer length N. Numerous numerical studies of lattice models[81,82] and continuous bead-stick or bead-spring models[83–86] suggest empirically a scaling ansatz motivated from polymer solutions in the Flory-Huggins mean-field theory,

$$T_\theta(N) - T_\theta = \frac{a_1}{\sqrt{N}} + \frac{a_2}{N}\,, \tag{27}$$

where $T_\theta = \lim_{N\to\infty} T_\theta(N)$.

Alternatively, field-theoretic considerations predict in three dimensions, where the tricritical collapse transition is at its upper critical dimension, a multiplicative logarithmic correction on the leading term,[87–93]

$$T_\theta(N) - T_\theta = \frac{A}{\sqrt{N}(\ln N)^{7/11}}. \tag{28}$$

Parsons and Williams[83,84] have claimed that their data confirm the field-theoretic prediction (28), but the majority of studies[81,82,85,86] favors the simpler scaling ansatz (27).

Estimates for $T_\theta(N)$ can be obtained from the peak location of the temperature derivative of the squared radius of gyration. The curves shown in Fig. 5(a) are results from histogram reweighting of data obtained in multicanonical simulations and the data points with error bars are from time-series reweighting.[86] With increasing polymer length N, the peak height increases and the collapse transition shifts to higher temperatures. The scaling behavior with N is shown in Fig. 5(b) with the solid line representing a fit with the ansatz (27) (with non-universal parameters $T_\theta = 2.646(4)$, $a_1 = -8.11(6)$, and $a_2 = 7.1(2)$). The important result is that very different models exhibit the same qualitative finite-size scaling behavior and are thus expected to describe the same generic properties with respect to the collapse transition.[19]

3.1.5. *Semiflexible polymers*

With additional bending stiffness the conformational statistical physics of *semiflexible* polymers becomes much richer than that of a flexible polymer.[94,95] This is not only because here next to temperature (or, equivalently, solvent condition) also the bending stiffness κ is an independent second parameter, but the emerging structural motifs are much more multifaceted than for a flexible polymer. They range from rod-like, collapsed,

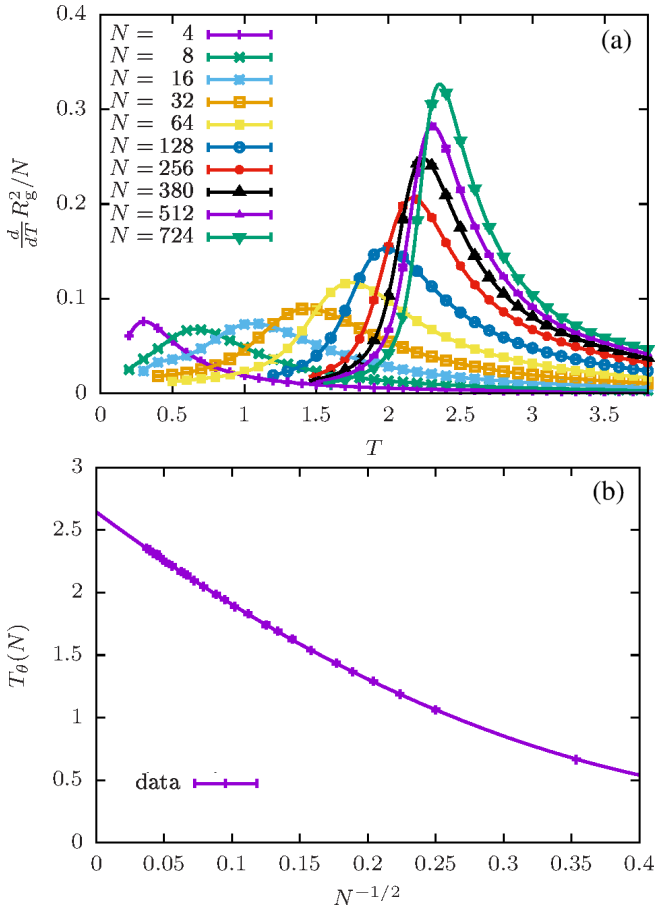

Fig. 5. (a) The canonical temperature derivative of the squared radius of gyration for the bead-spring polymer with non-bonded Lennard-Jones interaction. (b) Finite-size scaling of the collapse transition temperature. The data is nicely described by the solid line representing the ansatz (27) (taken from Ref. 86).

frozen, bent, hairpin, and toroidal structures to stable knots of various types.[95]

In order to map out the phase diagram in the $T-\kappa$ plane we performed two types of Monte Carlo studies in generalized ensembles. For the first type, we developed a combination of multicanonical simulations with parallel tempering in the κ direction, and the second set of simulations is based on a two-dimensional variant of parallel tempering with replica exchanges

in both T and κ.

The reason for employing such combinations is that also multicanonical simulations can still get stuck when there are barriers in configuration space that are not reflected in the energy distribution $p(E)$, but rather in observables "orthogonal" to E. To cope with this problem, we combined the multicanonical method in the energy direction with parallel tempering in an "orthogonal" direction,[96] which here corresponds to the bending energy parametrized by κ. From the view point of parallel tempering the only difference to the standard aproach is that now the underlying Monte Carlo algorithm is a multicanonical simulation at κ_μ based on a weight $W_\mu(E)$ instead of the canonical Boltzmann factor $\exp(-\beta_\mu E)$. The replica-exchange probability (18) hence generalizes to ($E_{1,\mu} = E_1(x_\mu)$ etc.)

$$p_{\rm acc}\left(x_\mu \leftrightarrow x_\nu\right) = \min\left(1, \frac{W_\mu(E_{1,\nu}+\kappa_\mu E_{2,\nu})W_\nu(E_{1,\mu}+\kappa_\nu E_{2,\mu})}{W_\mu(E_{1,\mu}+\kappa_\mu E_{2,\mu})W_\nu(E_{1,\nu}+\kappa_\nu E_{2,\nu})}\right) . \quad (29)$$

While this is conceptually quite straightforward, the actual implementation of an efficient computer code is rather cumbersome.

Somewhat simpler is the two-dimensional parallel tempering variant. Assuming that the energy can be written as $E = E_1 + \kappa E_2$, one performs simulations with any legitimate Monte Carlo algorithm at m different parameter pairs $(\beta,\kappa)_\mu$ of the system in parallel and proposes with a certain frequency configuation exchanges $x_\mu \leftrightarrow x_\nu$. These are accepted with probabilty (18) with $\Delta\beta\Delta E \to \Delta\beta\Delta E_1 + \Delta(\beta\kappa)\Delta E_2$. In this two-dimensional parameter space (here β or T and κ), it is easier to circumvent "hidden" topological barriers which otherwise could hinder the one-dimensional flux of the replicas. To obtain the optimal spacings of the simulations points in the two-dimensional parameter space and the optimal exchange frequencies is quite a tricky task, but with some trial and error procedure one can usually achieve a stable and well working (albeit presumably only sub-optimal) simulation set-up.

Using these two combined generalized-ensemble methods we have performed extensive simulations of a semiflexible polymer with $N = 14, 28$, and 42 monomers.[95,97–99] Figure 6 shows the phase diagram for the 28mer. The transition lines were determined by measurements of the two subenergies $\langle E_{\rm LJ}\rangle$ and $\langle E_{\rm Bend}\rangle$, the squared end-to-end distance $\langle R_{ee}^2\rangle$, the squared radius of gyration $\langle R_{\rm gyr}^2\rangle$, and the eigenvalues of the gyration tensor $\langle\lambda_1\rangle$, $\langle\lambda_2\rangle$, and $\langle\lambda_3\rangle$. Peaks of the temperature derivative of these observables for a given bending stiffness κ then mark the transition lines in Fig. 6. Due to the finite length of the polymer, different observables give slightly different

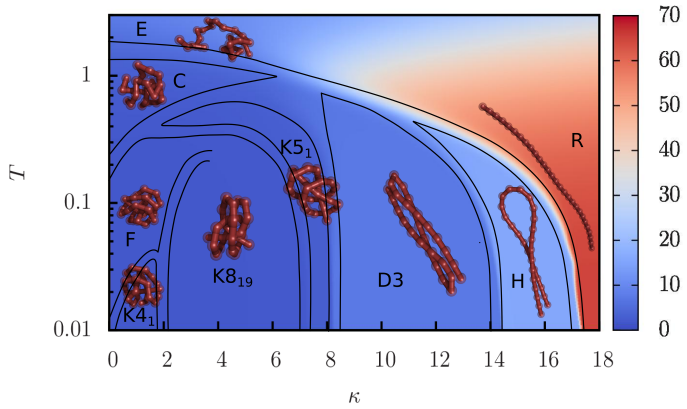

Fig. 6. Bulk phase diagram of a semiflexible 28mer in the temperature (T) – bending stiffness (κ) plane (E: elongated, R: rod-like, C: collapsed, F: frozen, K: knotted, DN: N aligned strands, H: hairpin). The background color encodes $\langle R^2_{\rm gyr}\rangle$. Note that the temperature is given on a logarithmic scale (taken from Ref. 95).

transition temperatures, which is reflected by the width between the black lines. So, strictly speaking, one should call a "transition" more precisely "pseudotransition" and a "phase diagram" rather "pseudophase diagram", but for brevity the term "pseudo" will be omitted in the following. The background color of Fig. 6 encodes the average extension of the polymer in terms of $\langle R^2_{\rm gyr}\rangle$.

As the most intriguing observation one notes that the phase diagram features stable phases that are characterized by knotted polymer chains (denoted by K). Two examples are depicted in Fig. 7. The other structural motifs (R: rod-like, C: collapsed, F: frozen, DN: bended with N aligned strands, H: hairpin) are similar to those found in a quite similar bead-*spring* model,[94,100] where the stable knot phases, however, have not been observed.

Closer inspection reveals that these knots can be identified as $C_n = 4_1$, 5_1, and 8_{19} knots, where in the usual classification scheme C counts the minimal number of crossings of any projection of a knot onto a two-dimensional plane and the subscript n distinguishes topologically different knots with the same C. It is interesting to note that 5_1 and 8_{19} knots are so-called torus knots, which are known to be preferentially formed in viral DNA.[101] This is discussed in more detail in Chapter YY of this book by

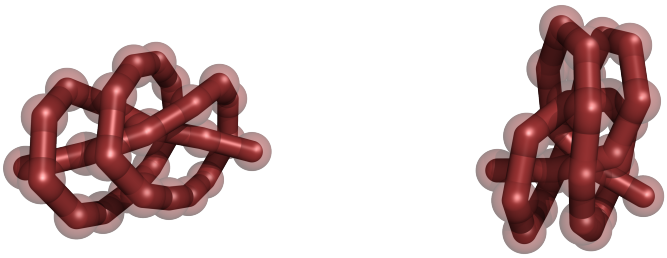

Fig. 7. Typical knots of types 5_1 (at $\kappa = 7.50$, $T = 0.045$) and 8_{19} (at $\kappa = 6.10$, $T = 0.035$) obtained for a semiflexible 28mer.

Sergei Nechaev. For identifying the knot type given the coordinates of the conformation, we employed a method described in Ref. 102, where a specific product $\Delta_p(t) \equiv |\Delta(t) \times \Delta(1/t)|$ of the Alexander polynomial $\Delta(t)$ is evaluated at $t = -1.1$. For the definition of the Alexander polynomial and a comprehensive exposition of mathematical knot theory, an excellent reading is the textbook by Kauffman.[103]

Mathematically, however, the identification of knots in *open* polymers is not well defined. The identification of knots in open polymers hence requires some empirical prescription of how to close its two ends virtually. If one would just connect the two termini by a straight line, this would result in quite complicated knots when the polymer is very compact. This clearly must be considered as an artefact. We therefore employed the more sophisticated closure sketched in Fig. 8, which is inspired by tying a real knot. First one connects the termini by a straight line, which is then extended in both directions to the virtual end points A' and B' far away from all monomers. The polymer is then closed via straight lines connecting A' and B' with a far away point C on the perpendicular bisector of the connecting line. We checked that this procedure is numerically stable, i.e., any reasonably defined closure results with high probability in the same knot type.

Finally we come back to the remark at the beginning of this subsection that "hidden" barriers in "orthogonal" directions may hamper multicanonical simulations and hence require more sophisticated combined simulation algorithms. The underlying physical orign of this problem can be nicely illustrated by the transitions from the frozen or bent phases into the knot phases which at first sight exhibit quite an intriguing behavior. As tran-

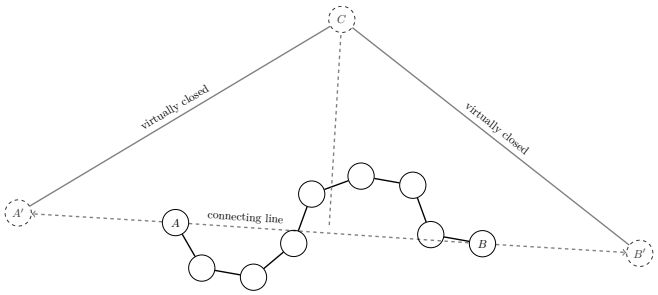

Fig. 8. Sketch of the employed prescription to close an open polymer virtually.

sitions between two structured states, one would expect them to behave first-order-like, similar to other solid-solid transitions. A glance at the inset of Fig. 9 for the D3–$K5_1$ transition suggests, however, that this expectation is not fulfilled since the energy distribution $p(E)$ exhibits only a single peak. There is no indication for the typical double-peak structure at a first-order-like phase transition and hence no signal of latent heat.[104,105] The true nature of the transition is only revealed when one considers the *two-dimensional* energy distribution $p(E_{\rm LJ}, E_{\rm Bend})$, for which indeed two clearly separated peaks are visible in Fig. 9.[95] The peak in front corresponds to the (unknotted) bent phase D3 and the other in the back to the knot phase $K5_1$. The reason is that the total energy E happens to be just the projection along the diagonal of the two-dimensional distribution for which the two peaks fall on top of each other.[95] This observation explains why only a single peak shows up in $p(E)$ and no latent heat is detectable. Figure 9 is thus a good example for concealed barriers along an "orthogonal" direction, which prompted us to develop the more elaborate combined generalized-ensemble algorithms.

3.2. *Polymer adsorption*

For many applications like surface coatings or colloidal stabilization, the behavior of polymers at interfaces is of high relevance, as is also true for the interaction of proteins with surfaces. From the basic science point of view, single chains at surfaces introduce an interesting competition between three-dimensional phase transitions, two-dimensional phase transitions and the adsorption transition of the chains onto the surface. For this reason in the last ten years many generalized ensemble Monte Carlo simulations have been devoted to this problem.

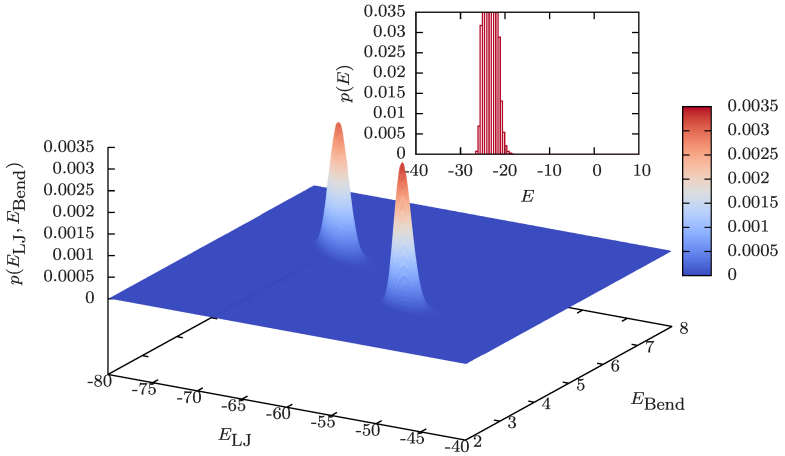

Fig. 9. Two-dimensional energy histogram $p(E_{\rm LJ}, E_{\rm Bend})$ of a 28mer at the D3–K5$_1$ transition for $\kappa = 8.0$ at $T = 0.18$, signaling clear phase coexistence. The inset shows the one-dimensional energy histogram $p(E)$ of the total energy $E = E_{\rm LJ} + \kappa E_{\rm Bend}$, which corresponds to a projection along the diagonal of the two-dimensional histogram. In this projection, the two peaks fall on top of each other, so only a single peak is visible in $p(E)$.

3.2.1. *Flexible polymer adsorbing onto a flat substrate*

Two lines of approach have been followed in these investigations: In the first one, a single polymer chain next to a flat, attractive substrate and confined by a second parallel, steric (i.e., non-interacting) wall at sufficiently large distance to the substrate has been studied. This may be viewed as geometric confinement in a slit geometry, but in the present context the second inert, steric wall at "sufficient distance" is mainly added for technical reasons in order to keep the translational degrees of freedom orthogonal to the substrate under control. In the second line, tethered chains with one end grafted to the attractive substrate in an infinite half-space have been analyzed, the classical model for studying the adsorption transition in polymer physics. Both approaches differ in the contribution of the translational entropy of the chain, which depends on the distance between the two confining walls in the slit geometry.

For homopolymer chains, the slit geometry has been investigated for a two-dimensional system in Ref. 106 and for a three-dimensional system

in Refs. 107–112, whereas the end-grafted case has been studied in Refs. 113–116,118. In both cases the three phases in 3d, coil, liquid globule and ordered globule (for large enough interaction range) exist also in this case, but in addition for very strong attraction to the surface, the quasi two-dimensional chains show the corresponding 2d phases (however, the nature of the 2d crystallization transition of single polymer chains has not been analyzed yet). The two regimes are separated as a function of attraction strength to the surface by the adsorption transition. Close to this critical value of the surface attraction, the chains are adsorbed but not completely two-dimensional leading to further layering transitions, especially of adsorbed ordered structures.

A typical phase diagram of states for a polymer chain at an attractive wall is shown in Fig. 10. Adsorbed phases are indicated by the letter "A", desorbed by "D", extended states by "E", globular states by "G" and compact ordered states by "C". This result has been obtained for a generic coarse-grained bead-stick model of a linear polymer with fixed bond length (normalized to unity) where three terms contribute to the energy:[118]

$$E = 4\epsilon_{\rm LJ} \sum_{i=1}^{N-2} \sum_{j=i+2}^{N} \left[\left(\frac{\sigma}{r_{ij}} \right)^{12} - \left(\frac{\sigma}{r_{ij}} \right)^{6} \right] + \frac{1}{4} \sum_{i=1}^{N-2} (1 - \cos\vartheta_i) + \epsilon_s \sum_{i=1}^{N} \left[\frac{2}{15} \left(\frac{\sigma_s}{z_i} \right)^{9} - \left(\frac{\sigma_s}{z_i} \right)^{3} \right] . \tag{30}$$

The first two terms are the energy of a polymer in bulk that consists of the standard 12–6 Lennard-Jones (LJ) potential and a (very) weak bending energy, where r_{ij} denotes the distance between the monomers i and j and $0 \le \vartheta_i \le \pi$ the bending angle between adjacent bonds. The third term describes the interaction with the flat attractive substrate in the xy-plane, where z_i is the distance of the ith monomer to the surface. The specific form of the interaction is obtained by following Ref. 117 in treating the substrate as a continuous medium and integrating over the half-space $z \le 0$, where every space element is assumed to interact with a single monomer by the standard 12–6 Lennard-Jones expression. The energy scale is fixed by setting $\epsilon_{\rm LJ} = 1$, and also the length scales σ and σ_s are both set to unity. The adsorption strength is controlled by the parameter ϵ_s which weighs the magnitude of the monomer-surface and monomer-monomer interactions.

The main difference between the slit geometry and the end-grafted case occurs for the adsorption transition. In our studies[108–110] we observed that the adsorption transition in the slit geometry can be first-order-like

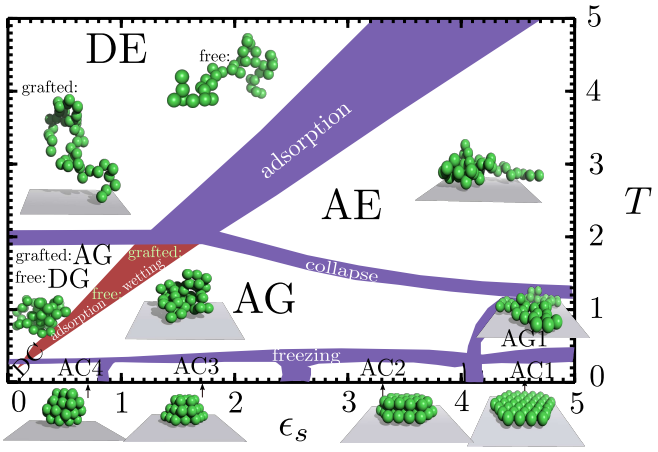

Fig. 10. Qualitative phase diagram of homopolymer chains next to an attractive surface moving either freely in a three-dimensional slit geometry ("free") or in a tethered geometry where one end of the polymer is fixed on the surface ("grafted") (taken from Ref. 118).

for short chains, turning second-order-like in the thermodynamic limit of infinite chain length. This is in contrast to the end-grafted case, where this transition exhibits always second-order-like signatures. The difference is caused by the importance of the translational entropy in the slit case. We furthermore argued that the adsorption temperature for chains of length N in the slit geometry should be inversely proportional to $N^{-1} \ln L_z$, where L_z is the distance between the walls. For every fixed chain length N, the transition temperature in the slit geometry therefore approaches zero in the dilute limit $L_z \to \infty$. For a related study comparing canonical and microcanonical analysis of nongrafted homopolymer adsorption, see Refs. 119,120.

The nature of this phase diagram also did not depend on whether a short-ranged[107,113,114] or long-ranged[108–110,116] van der Waals like attraction to the substrate was used. A simulation at finite, adjustable concentration (i.e., distance L_z between the walls) of a simplified model for a polyelectrolyte in solution with its counter ions was performed by Volkov *et al.* (Ref. 112) where they determined a two-dimensional density of states $g(E, V)$ depending on energy and volume.

3.2.2. *Flexible polymer inside a curved cavity*

The main adsorption properties are also preserved when one considers a flexible polymer confined inside a spherical cavity and attracted by the inner wall of the sphere.[121–123] For a sketch of this situation, which mimicks a polymer confined in a biological cell, see Fig. 11(a). Here the usually employed 9–3 Lennard-Jones surface potential for a flat substrate (obtained from a *three*-dimensional integration of a 12–6 Lennard-Jones potential over the lower half space $z \le 0$) has to be replaced by a 10–4 Lennard-Jones surface potential (resulting from a *two*-dimensional integration over the spherical surface). This yields the somewhat complicated looking expression[124]

$$V_{\rm s}(r_i) = 4\pi\epsilon_c \frac{R_c}{r_i}\left\{\frac{1}{5}\left[\left(\frac{\sigma}{R_c - r_i}\right)^{10} - \left(\frac{\sigma}{R_c + r_i}\right)^{10}\right] - \frac{\epsilon}{2}\left[\left(\frac{\sigma}{R_c - r_i}\right)^{4} - \left(\frac{\sigma}{R_c + r_i}\right)^{4}\right]\right\}, \tag{31}$$

where the parameter ϵ in the second term defines the attraction strength of the spherical surface [notice that for consistency with other work, here we adopted a different convention than in Eq. (30)]. Still, the shape of the surface potential (31) looks qualitatively similar to that used in (30) as is demonstrated in Fig. 11(b). In fact, by an appropriate matching of the coupling constants ($\epsilon_s \approx (4\pi/1.054)(3/10)\epsilon^{5/3}$) it can be theoretically argued that this difference does not matter much,[124] and our multicanonical simulations do confirm this expectation.[121–123] This can be seen in Fig. 12 which shows the resulting phase diagram in the T–ϵ plane. Compared with Fig. 10 for the flat substrate, the scale on the x-axis is different and the transition lines are slightly tilted (recall the non-linear mapping between ϵ and ϵ_s), but the overall appearance of the phase structure is very similar. Representative conformations of the different phases for the attractive sphere system are depicted in Fig. 13.

3.2.3. *Flexible polymer adsorbing onto a patterned substrate*

The adsorption of polymers onto patterned attractive substrates is of high practical importance, for instance for sensor applications. As a first step in this direction we have studied in Ref. 125 the adsorption of a flexible homopolymer of length $N = 40$ onto a substrate with a regular stripe pattern. The effect of the stripe pattern is modeled by replacing the attraction strength ϵ_s of the 9–3 surface potential in Eq. (30) by a periodic

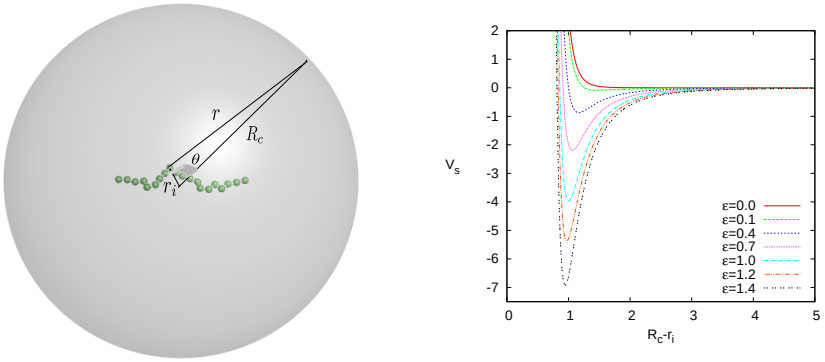

(a) (b)

Fig. 11. (a) Sketch of a freely circulating 20mer inside an attractive sphere of radius $R_c = 20$. (b) The attractive surface potential (31) with $R_c = 20$ for various values of ϵ. The location of the minimum varies from $R_c - r_i \approx 1.47$ for $\epsilon = 0.1$ to ≈ 0.95 for $\epsilon = 1.4$.

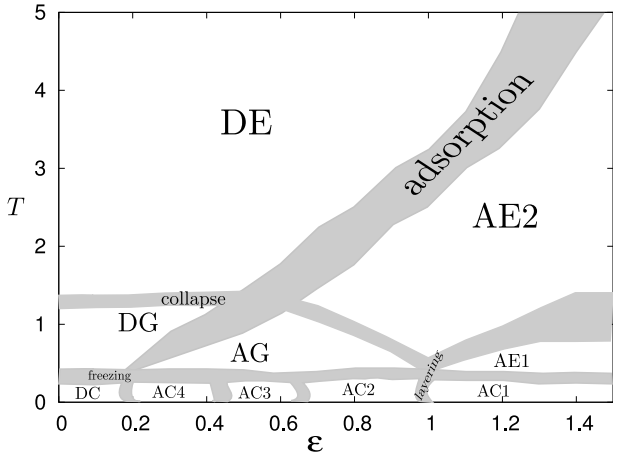

Fig. 12. Pseudophase diagram of the polymer-attractive sphere system in the temperature (T) – adsorption strength (ϵ) plane as obtained in Ref. 121. The labels "A/D" and "E", "G", "C" have the same meaning as in Fig. 10.

x-dependent adsorption-strength parameter

$$\epsilon_{\rm sub}(x) = \epsilon_{\rm s} + \epsilon_{\rm stripe} \begin{cases} \cos^2(\alpha(x)\pi), & \text{if } |\alpha(x)| \le 1/2, \\ 0, & \text{otherwise,} \end{cases} \tag{32}$$

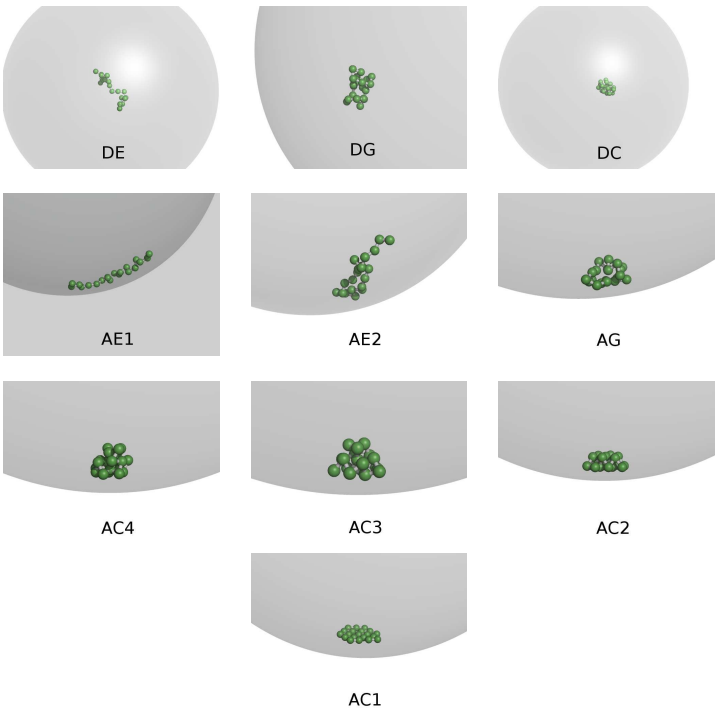

Fig. 13. Typical polymer conformations representative of the different phase as observed in the simulations of a flexible polymer confined in a sphere with an attractive surface.

where the choice $\alpha(x) = [(x/\sigma_x + 1/2) \mod D] - 1/2$ guarantees that the periodic potential is maximally attractive at the stripe locations $x_{\max}^{(k)} = \pm kD\sigma_x$ (k integer), smoothly decays towards $x_{\max}^{(k)} \pm \sigma_x/2$, and is zero otherwise.[b] As for all other length scales, we set $\sigma_x = 1$ in the simulations, and the distance between the stripes was chosen to be $D = 5$.

Figure 14 shows the resulting structural phase diagram for an overall attraction strength of the substrate of $\epsilon_s = 1$, i.e., identical to the non-bonded intramolecular energy scale $\epsilon_{LJ} = 1$. The limit $\epsilon_{stripe} = 0$ is hence identical to the cross-section at $\epsilon_s = 1$ in Fig. 10. This is why in the desorbed region only the DE and DG phases are present, but not DC. The most compact polymer structures are those with three layers in the low-temperature phase AC3. The adsorption phase diagram for a homogeneous

[b]The modulo operation $v \mod w$, where v, w are real numbers, is given by the floor function: $v \mod w = v - w\lfloor v/w \rfloor$, where $\lfloor a \rfloor$ is the largest integer not greater than a.

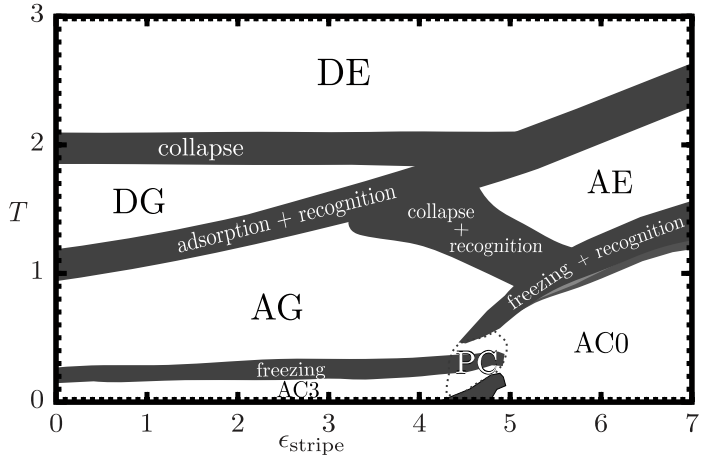

Fig. 14. Phase diagram of structural polymer phases for a substrate with stripe pattern, where $\epsilon_s = 1$ (from Ref. 125). The letters A/D denote phases where the polymer is preferentially adsorbed/desorbed. The second letters indicate increasing order in the A/D regions: expanded (E), globular (G), and compact (C); PC is short for "phase coexistence". Representative conformations are depicted in Fig. 15.

substrate in Fig. 10 is modified, because now the adsorption out of the different three-dimensional equilibrium structures (coil, globule, frozen) takes place with a competing recognition of the surface pattern by the polymer. In phase DE, entropy clearly dominates over non-bonded polymer energy and conformations are unstructured. Lowering the temperature leads to adsorption, but not ordering, i.e., the adsorption phase AE forms. The energetic attraction of the stripes is larger than that of the homogeneous regions of the substrate, so the polymer recognizes the existence of the stripes, but its typical extension is larger than the distance between two stripes. Therefore, the polymer structures attach to several stripes simultaneously, but in no specific way. For comparatively large stripe attraction strength ($\epsilon_{\text{stripe}} > 6$), the polymer undergoes a direct transition from AE to a singular regime that has no relevance on homogeneous substrates. This is the "rodlike phase" AC0 of linelike structures, where all monomers prefer contact with a single stripe (see Fig. 15).

Regarding the polymer structures, an obvious difference to the adsorption process on a homogenous substrate is that the polymer prefers the contact to the energetically more favorable stripe regions on the patterned substrate. For a comparison of typical conformations in the two cases, see

Fig. 15. Since the extension (radius of gyration in the xy plane) of the compact conformations in AG and AC3 is smaller than the distance between the stripes, the polymer recognizes exactly one stripe upon adsorption and the space between the stripes is virtually emptied, i.e., the AG/AC3 phases have a different appearance than their analogs in the homogeneous case. The adsorption transition from DG to AG is a docking process with no apparent refolding. This can also be traced back to the presence of the stripes since they reduce the translational entropy on the substrate.

An essential feature of stripe-patterned adsorption is the phase AC0, which can be interpreted as "topological" phase characterized by one-dimensional polymer structures, see Fig. 15. When going from AC0 to the compact phases AC3 respectively AG, a transition regime has to be passed that we denoted by PC (phase coexistence), where lamellar or film-like double-rod structures (which would make up a phase AC1) and double-layer or triple-rod structures (that would form a phase AC2) coexist with "pearl-necklace" structures as shown in Fig. 15.

The extended rod-like structures found for strong stripe attraction have also been observed in a variation to a hard-wall confinement where the phase behavior of a polymer chain next to a fluctuating (flat) membrane modeled as a square-net lattice was studied.[126] For very stiff membranes, our findings reproduced the behavior at a hard wall, as expected. For fluctuating membranes, on the other hand, a new adsorbed state occurred where the membrane tries to wrap around the adsorbed polymer. When the intramolecular interaction of the polymer wins, the membrane wraps around a compact, collapsed conformation. For strong attraction to the membrane, the chain adsorbed in an extended configuration maximizing the monomer-membrane contacts, see Fig. 16. Such behavior may depend on the local commensurability of the membrane and the polymer, however.

3.2.4. *Semiflexible polymer adsorbing onto a flat substrate*

Recently we extended these studies to semiflexible polymers interacting with a flat substrate,[127] using here the bead-spring model with FENE bonds and considering the case where the polymer (of length $N = 40$) is grafted with one end to the substrate. Since already the bulk phase diagram for a semiflexible polymer is much richer than for a flexible polymer, also the adsorption process is a much richer phenomenon in the semiflexible case that is governed by at least three control parameters: Temperature, surface attraction strength and bending stiffness. In Ref. 127 we decided to consider

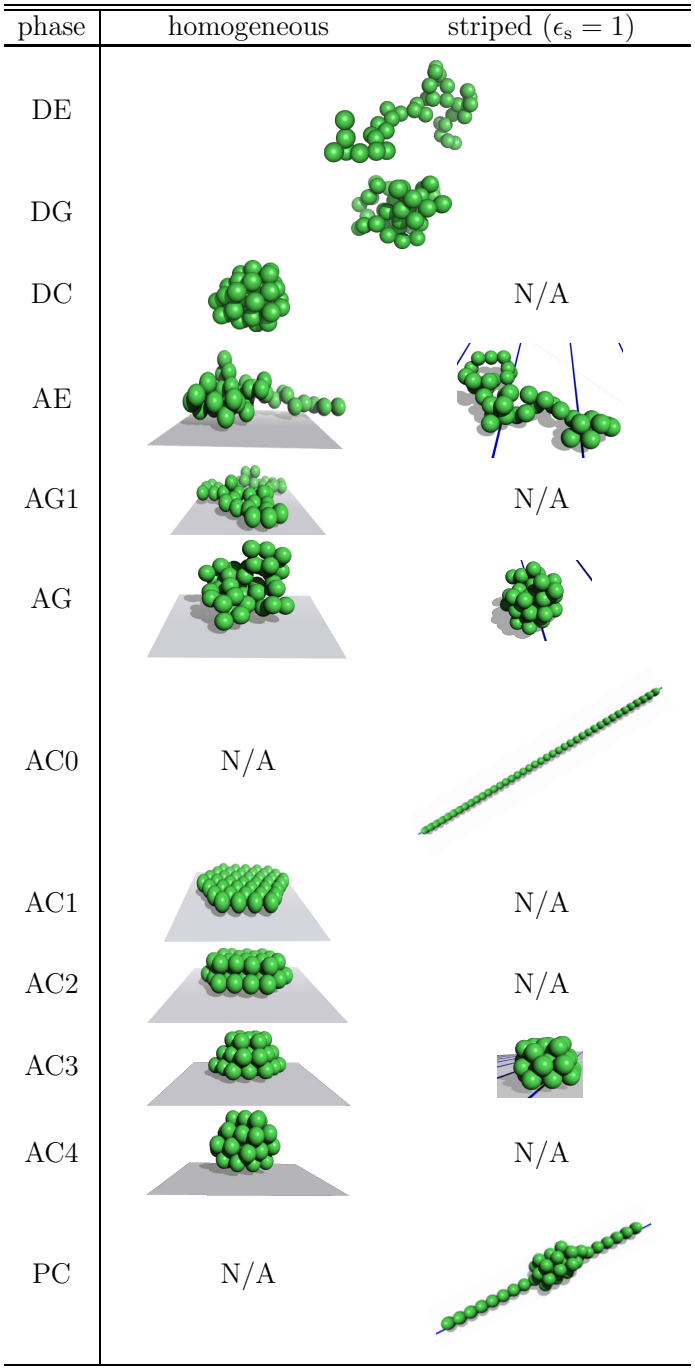

Fig. 15. Comparison of representative conformations in the different structural phases for homogeneous ($\epsilon_{\text{stripe}} = 0$) and striped substrates (with $\epsilon_s = 1$).

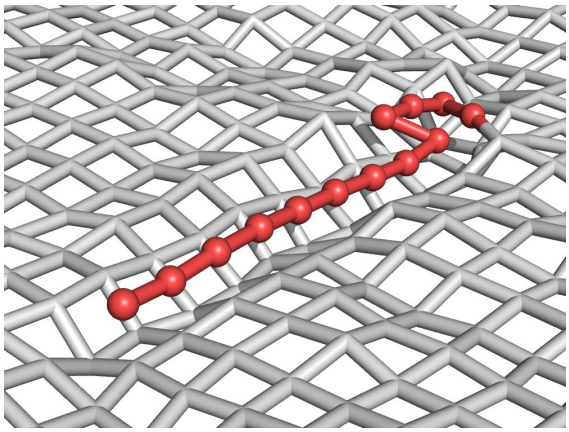

Fig. 16. Stretched conformation, incorporated into a fluctuating membrane. For these structures the membrane forms a channel into which the almost fully stretched polymer is embedded. The polymer is not randomly expanded here, but specifically elongated (taken from Ref. 126).

a few characteristic surface attraction strengths $\epsilon_s = 0, 0.7, 1.5$, and 5.0, and to construct the phase diagrams in the entire temperature–stiffness plane. Our result for $\epsilon_s = 0.7$ is shown in Fig. 17 together with characteristic polymer conformations in the different phases.

3.2.5. *Adsorption of a P3HT macromolecule to a gold substrate*

At a more quantitative level, we recently studied the adsorption properties of Poly(3-hexylthiophene-2,5-diyl) (P3HT) macromolecules to a (reconstructed) Au(001) surface by comparing our simulation results with experiments under ultra-high vacuum conditions. The choice of this specific polymer is motivated by its potential usefulness for photovoltaic applications as discussed, e.g., in Ref. 128. Its bulk properties are hence relatively well studied experimentally and also chemically realistic coarse-grained models are available in the literature. Our own simulational work[130] relies on the P3HT model of Ref. 136. The atomic structure of P3HT and the employed coarse-grained model are depicted in Fig. 18(a). The particles labeled by P1 represent thiophene rings along the polymer backbone (positioned in the center of mass of the rings). The particles labeled by P2 and P3 comprise the two parts of the methyl groups of a side chain (centered around the first respectively last three carbon atoms). The intramolecular forces are modeled by four terms: anharmonic bond vibrations

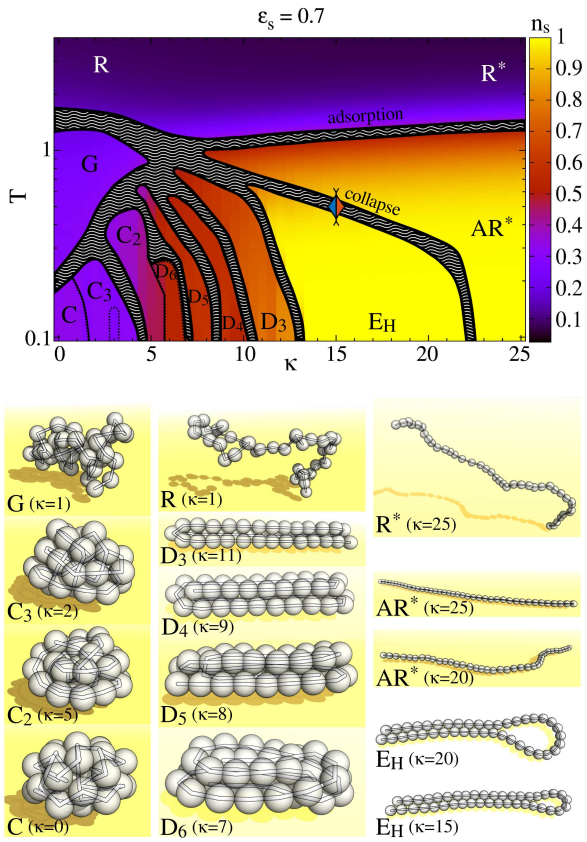

Fig. 17. Structural phase diagram for a semiflexible polymer of length $N = 40$ grafted to a weakly attractive substrate with surface attraction strength $\epsilon_s = 0.7$ (from Ref. 127. The background color encodes the average fraction of surface contacts $n_s = N_s/N$. The dotted lines indicate that phase transition signals are found only in a small subset of observables. Representative conformations of the respective conformational regimes are shown below: Random coil-like (R) and weakly bent rod-like (R* and AR*), compact (C), and globule-like (G) conformations, and folded bundles (D_m) as well as hairpins (E_H). The (blue-red) rhombus at $\kappa_x \approx 15$ marks the crossover from a second-order-like (small κ) to a first-order-like (large κ) collapse transition.

$U_{\rm bond}(l) = \sum_{i=2}^{n} c_i(l-l_0)^i$, bending energy $U_{\rm bending}(\Theta) = \sum_{i=0}^{n} c_i(\Theta-\Theta_0)^i$, torsion energy $U_{\rm torsion}(\Phi) = \sum_{i=0}^{n} c_i \cos^i(\Phi)$, and interactions $U_{\rm nb}$ between non-bonded particles. The latter include Lennard-Jones-like as well as Coulomb potentials, which are given in the supporting information of Ref. 136 in tabular form together with the $26 + 42 + 24 + 5 = 97$ parameters of

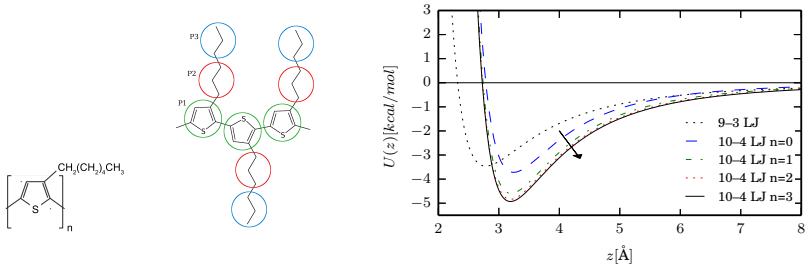

(a) (b)

Fig. 18. (a) The molecular structure of Poly(3-hexylthiophene-2,5-diyl) (P3HT) and its two-dimensional representation with overlaying coarse-grained particles: P1 is positioned at the center of mass of the thiophene ring. P2 and P3 each surround three carbon atoms of the side chain methyl groups. (b) Surface potential $U_{\rm surf}$ of an FCC crystal of Au particles interacting with a particle at a distance z from the surface as computed for (i) a homogeneous crystal (9–3 Lennard-Jones) and (ii) a crystal composed of n homogeneous layers (10–4 Lennard-Jones) separated by a distance Δz.

the explicit potentials.

The Au(001) surface is known to form a quasihexagonal reconstruction at the vacuum interface. As discussed in Ref. 133 (see in particular their Fig. 1) the height modulations of the atoms of the top-most hexagonal layer induce a stripe-like pattern of the substrate terraces. However, when studying particle interaction with a surface, Steele[117] argued that variations of the position of the interacting particle over the unit cell of the surface lead to differences in the effective potential. Since this difference is only observable at very small distances from the surface this effect has been neglected in the simulations, because of the size of the coarse-grained particles used here. This allows for a coarse-graining of the surface as well. In the simplest approach one would use a 9–3 Lennard-Jones potential as in the generic model (30). This potential, however, underestimates the distance of adsorbed particles to the surface. An improved surface potential was proposed in Ref. 135. Instead of integrating over the entire z-half-space, a (two-dimensional) integration is performed over layers of the substrate, giving the potential

$$U_{\rm surf,10-4}(z,n) = 2\pi\epsilon\rho\Delta z\sigma^2 \times \left[\frac{2}{5}\left(\frac{\sigma}{z+n\Delta z}\right)^{10} - \left(\frac{\sigma}{z+n\Delta z}\right)^{4}\right], \quad (33)$$

where ρ is the atom number density of the substrate material, n the layer number, and Δz the distance between neighbouring layers. A

comparison of the 9–3 Lennard-Jones potential and the layer potentials is shown in Fig. 18(b). In principle, one would have to sum over an infinite number of layers, but usually the sum converges very quickly. This leads to the coarse-grained surface potential $U_{\rm surf}(z) = U_{\rm surf,10-4}(z_0,0) + \sum_{n=1}^{3} U_{\rm surf,10-4}(z,n)$. The 12–6 Lennard-Jones parameters $\epsilon_{\rm Au} = 5.29\,{\rm kcal\,mol^{-1}}$ and $\sigma_{\rm Au} = 2.629\,{\rm \AA}$ for the gold atoms were taken from[134] and the atom number density of gold was computed to be $\rho = 0.059\,{\rm \AA^{-3}}$ at room temperature. For the coarse-grained particles we used the atomistic 12–6 Lennard-Jones parameters from Ref. 136: S1 for P1, C4 for P2 and P3. Combined interaction parameters were computed using the rules of Ref. 137, $\sigma_{ij} = \left[\left(\sigma_{ii}^6 + \sigma_{jj}^6\right)/2\right]^{1/6}$, $\epsilon_{ij} = 2\sqrt{\epsilon_{ii}\epsilon_{jj}}\sigma_{ii}^3\sigma_{jj}^3/\left(\sigma_{ii}^6 + \sigma_{jj}^6\right)$, since they are known to produce better results for rare gases than the often employed Lorentz-Berthelot rules

Figure 19(a) shows typical room-temperature scanning tunneling microscopy (STM) images of the Au(001) surface after in situ ultra-high vacuum (UHV) electrospray deposition of individual P3HT molecules. Two terraces can be seen separated by a monoatomic step running from the upper center to the lower left corner of the image. On top of the terraces a closer look reveals a stripe-like modulation which results from the aforementioned quasihexagonal reconstruction of the Au(001) surface.

The Monte Carlo simulations were run for 10^7 sweeps, after 10^6 sweeps to equilibrate all bond and torsion angles. Errors were obtained with the standard binning method. For comparison with the experimental data only a single-monomer displacement update was employed, since this update is close to a realistic particle movement on the surface. More advanced Monte Carlo update moves (such as pivot rotations), however, help to reach equilibrium states faster. In the top row of Fig. 19(b) characteristic conformations of a chain with 60 monomer units are shown. The experimental STM image on the left-hand side shows an elongated slightly curved chain which makes seven turns. A comparable configuration taken from the simulation is shown in the lower row, indicating that a small bending of the chain can arise from a local rearrangement of the side chains. However, a stronger curvature of the molecule is connected to a local trans-cis isomerization. The four black points along the chain in Fig. 19(b) mark the positions where single thiophene rings are flipped which, in turn, induces a bending of the chain. The hairpin-like collapsed structure of the upper right image shows the same polymer recorded 45 min earlier. Overall the experimentally observed chain conformations are in good qualitative agreement with

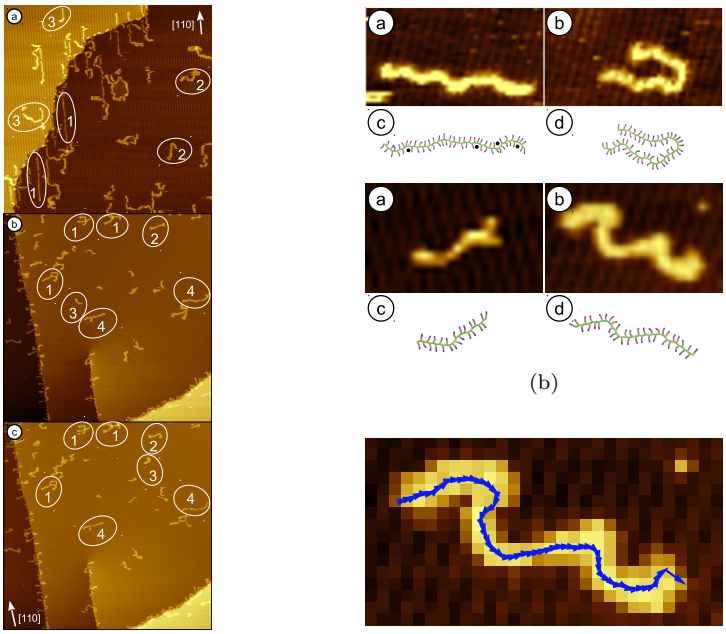

Fig. 19. (a) Three STM images taken 15 min apart of in situ deposited P3HT molecules on an Au(001) surface (for further explanation see Ref. 130). (b) Comparison of experiment (upper rows) and simulation (lower rows). Top: Elongated coil and collapsed hairpin conformations of a 60 monomer chain where the flipped side chains are marked with black dots. Bottom: Typical conformations of P3HT chains with 25 (left) and 40 (right) monomers. (c) Example for tracing the P3HT polymers in the STM images for extracting the statistical information.

selected chain conformations obtained from the simulations despite the fact that the substrate is strongly simplified and no geometrical constraint on the molecular orientation due to the stripe pattern could be observed.

For a quantitative comparison, we[130] focused on a statistical evaluation of the random-coil like two-dimensional conformations of the adsorbed P3HT molecules traced in the STM images as illustrated in Fig. 19(c). Useful quantities are the average two-dimensional squared radius of gyration $\langle R^2_{\mathrm{gyr,2d}}\rangle$ and the average end-to-end distance $\langle R_{\mathrm{ee}}\rangle = \langle|\vec{r}_N - \vec{r}_1|\rangle$ of the P3HT chains which are compared with simulation results in Fig. 20.

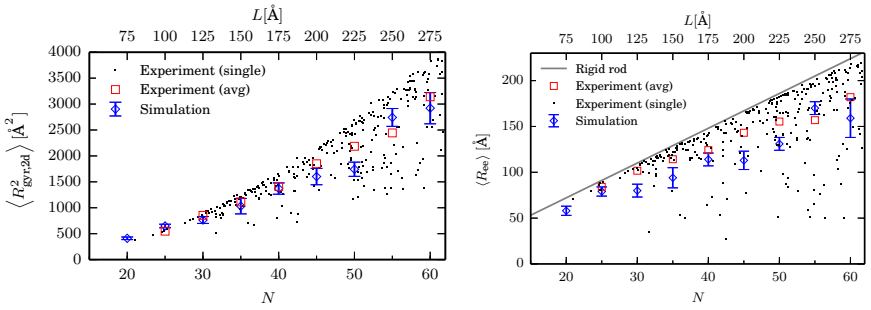

Fig. 20. Comparison of the two-dimensional (a) squared radius of gyration $\langle R^2_{\mathrm{gyr,2d}} \rangle$ and (b) the end-to-end distance $\langle R_{\mathrm{ee}} \rangle$ as obtained in Ref. 130 from experiment and simulation as a function of the monomer number N.

3.3. *Polymer aggregation*

Folding of proteins or the collapse of polymers are among the most prominent phase transformations of single macromolecules. In general, for an ensemble of a few interacting proteins or polymers also the interplay with aggregation plays an important role. In fact, for biopolymers, aggregation is one of the most relevant molecular structure formation processes. An important and extensively studied example is the extracellular aggregation of the $A\beta$ peptide, which is associated with Alzheimer's disease.

3.3.1. *Hydrophobic-polar (HP) peptide model for heteropolymers*

Aiming at an understanding of the basic mechanism of this process, we considered a coarse-grained bead-stick hydrophobic-polar (HP) model in the continuum (also often referred to as "AB model"),[138,139] where each residue is represented by only a single interaction site (the "C^α atom"). In this study, we have concentrated on a short 13mer with sequence $AB_2AB_2ABAB_2AB$ (representing a Fibonacci sequence) whose single-chain properties were already well studied.[140] The intermolecular interactions among the various peptides were assumed to be of the same 12–6 Lennard-Jones type as the intramolecular interactions among the monomers or residues of a single peptide. By confining M peptide chains in a cubic box of edge length L (= 40) with periodic boundary conditions, the relevant phase space could be completely covered by multicanonical simulations. This allows one to analyze the system from both the canonical and microcanonical

perspective.[138,139,141] In order to distinguish between the fragmented and aggregated regime, an order parameter $\Gamma^2 = \sum_{i,j} \left(\vec{r}_{\rm cm}^{\,i} - \vec{r}_{\rm cm}^{\,j}\right)^2 / 2M^2$ (with implicit minimal-distance convention for periodic boundary conditions) was introduced that adopts the definition of the squared radius of gyration for a single polymer and basically measures the average spread of the center-of-mass distances $|\vec{r}_{\rm cm}^{\,i} - \vec{r}_{\rm cm}^{\,j}|$ of the M chains $i = 1, \ldots, M$. In the aggregated phase, one thus expects $\Gamma^2 \approx 0$, whereas in the fragmented phase Γ^2 approaches a non-zero value.

Measuring the energy and specific heat as well as Γ^2 and its temperature derivative for systems with 2, 3, and 4 peptides, clear evidence for a first-order-like aggregation transition was obtained. For all three systems considered, the general behavior turned out to be similar. There is only this single transition which indicates that conformational changes of the individual peptides accompany the aggregation process and are not separate transitions, i.e., the hydrophobic core formation and the aggregation transition happen at the same temperature. A closer look for the 4-peptides system revealed, however, that the microcanonical entropy and temperature derived from the multicanonical data are so sensitive that a hierarchy of sub-phases in the nucleation transition region can be resolved.[142] Physically these sub-phases can be interpreted as signal that the next peptide starts to join the aggregate. Using similar techniques also the intra-association of hydrophobic segments in a 62 segment heteropolymer chain has been investigated.[143] In Ref. 144 the microcanonical thermostatistics of two isoforms of the amyloid β-protein (the Src SH3 domain and the human prion protein hPrP) was studied by using a coarse-grained model. Emphasis was laid in this work on free-energy barriers and the latent heat in these models, characterizing the amyloidogenic propensity, that is how aggregation-prone the heteropolymers are.

3.3.2. *Flexible homopolymers*

In another multicanonical simulation for four flexible homopolymer chains of length $N = 13$ (using the same model as above and formally the sequence A_{13}) it was observed that also in this case the collapse into the globular state and the aggregation transition happen at the same temperature.[145] In fact, to a good approximation, the aggregated state of M polymers of length N may be viewed as the collapsed globular state of a single polymer of length MN, which explains this coincidence. Along similar lines the aggregation properties of two coarse-grained bead-stick polymers of length

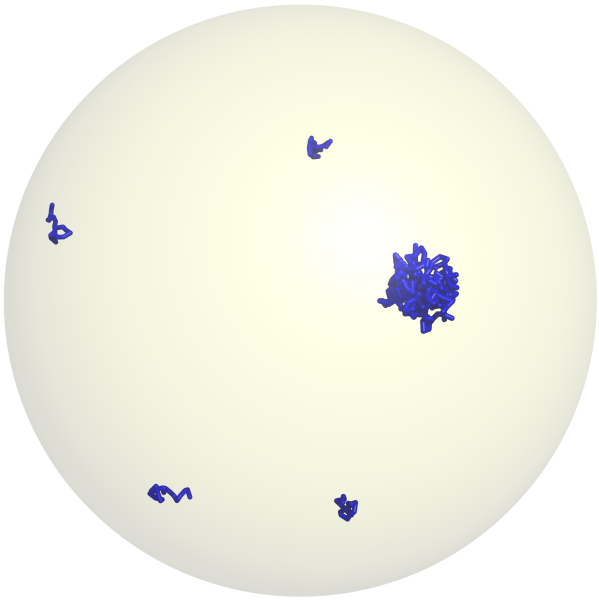

Fig. 21. Snapshot of a polymer system with $M = 20$ flexible polymers of length $N = 20$ confined in a spherical cavity radius $R_s = 30$ taken in the final production run of a multicanonical simulation (from Ref. 147). The displayed conformation corresponds to an intermediate state inside the aggregation-transition region.

$N = 22$ has been studied in Ref. 146. More recently this finding has been confirmed and extended in a more elaborate parallel multicanonical study of up to 24 flexible bead-spring polymers of length $N = 13, 20$, and 27 confined in a spherical cavity as depicted in Fig. 21.[147] Here the elasticity of the covalent bonds is governed by the finitely extensible nonlinear elastic (FENE) potential $V_{\rm FENE}(r) = -\frac{K}{2}R^2 \ln\left(1 - [(r - r_0)/R]^2\right)$ with $r_0 = 0.7$, $R = 0.3$, and $K = 40$.

In this study particular emphasis was laid on the analogy of the polymer aggregation process to particle condensation[47,148,149] and the finite-size scaling properties of the aggregation transition. Particle condensation, the equilibrium droplet formation in a supersaturated particle gas, is the paradigm of nucleation processes. For this case, theory, computer simulations and partially rigoros work predict that a first-order condensation-evaporation transition separates a homogeneous gas phase from an *inhomogeneous* phase, where a single macroscopic droplet of size N_D is in

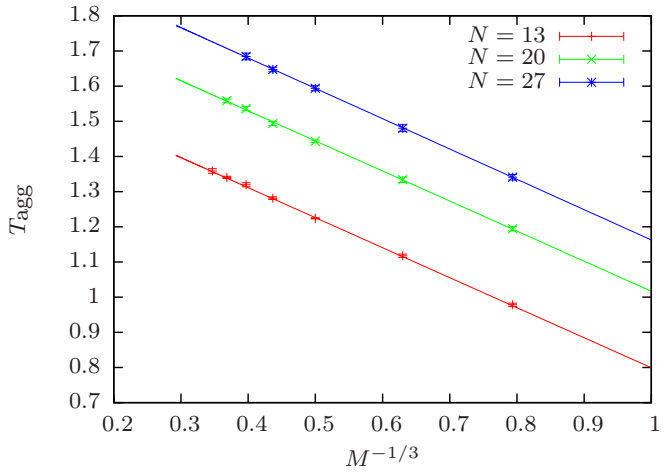

Fig. 22. Fits of the finite-size effects of the aggregation temperature for polymers of length N at density $\rho = 0.001$ as function of $M^{-1/3}$, where M is the number of constituents (taken from Ref. 147).

equilibrium with the remaining vapour.[150–155] In fact, the probability for intermediate-sized droplets was shown to be vanishingly small.[152,153] In the vicinity of the transition, the energy-dominated inhomogeneous condensed phase coexists with the entropy-dominated homogeneous gas phase. The transition between the two phases occurs by energy variation upon nucleation or dissolution. One consequence is that, at fixed density, the aggregation temperature $T_{\rm agg}$ is predicted to scale with the number of constituents M as $T_{\rm agg}(M) = T_{\rm agg}(\infty) + aM^{-1/4}$. However, as shown in Fig. 22, this was not observed for the considered system sizes. Rather a scaling $\propto M^{-1/3}$ fitted the data much better, which would be the expected result if either none or *all* polymers would aggregate. In other words, for such small systems the predicted heterogeneous condensed phase with a macroscopic aggregate or droplet in equilibrium with the surrounding vapour could not be confirmed numerically.

This prompted us to first reanalyze the simpler particle case,[149] where it is much easier to observe a possible crossover behavior when going from a small to a large number of constituents. Since our data for the particle case indeed confirmed such a crossover, this motivated us to increase the number of constituents in the polymer case considerably to $M = 64$ 13mers.[156] In this multicanonical study we could then observe the expected crossover

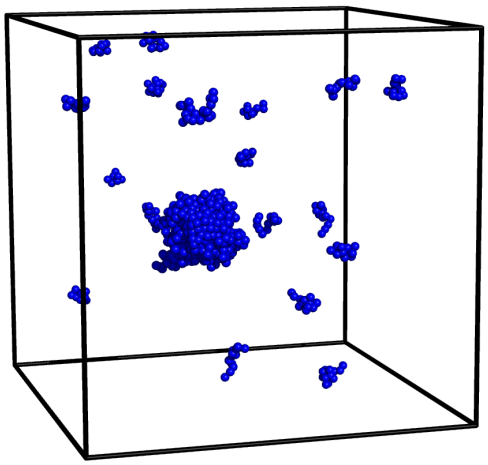

Fig. 23. Snapshot of a polymer aggregate in a dilute solution ($\rho = 0.01$). Shown is a cluster or aggregate of 64 bead-spring polymers with 13 monomers each in the droplet phase (taken from Ref. 156).

also for flexible polymers and hence confirm the theoretically predicted asymptotic finite-size scaling of the aggregation temperature $\propto M^{-1/4}$, using finite-size scaling fits with higher-order correction terms of the form $T_{\rm agg}(M) = T_{\rm agg}(\infty) + aM^{-1/4} + bM^{-1/2} + cM^{-3/4}$. Moreover, in Ref. 156 we could also determine the free-energy landscape associated with the first-order aggregation transition and measure the associated free-energy barrier $\beta\Delta F = \tau_{\rm eff} N^{1/2} + \text{const.}$, where $\tau_{\rm eff}$ is the effective interfacial free energy. The microcanonical analyses tool played again an important role in this study, where we applied it to both, the microcanonical ensemble with constant *potential* energy E_p (the commonly considered case in Monte Carlo computer simulations) and the ensemble with *constant* total energy E (the "real" microcanonical ensemble discussed in any textbook on statistical physics).

3.3.3. *Semiflexible homopolymers*

Building on this earlier work mainly for flexible polymers,[138,139,145,147] we have recently conducted a systematic investigation of the influence of bending stiffness on the polymer aggregation process.[157] In this study the same coarse-grained bead-spring model with FENE bonds was employed as in Ref. 147, and again it was assumed that the intra- and intermolecular interactions are identical and of 12–6 Lennard-Jones type. As for flexible polymers, the aggregated and separated phases of M semiflexible polymers can be monitored by the "phase" separation order parameter Γ^2. To distinguish in the aggregated phase for semiflexible polymers amorphous from bundle-like structures, a nematic-like end-to-end correlation order parameter $C_R = \frac{2}{M(M-1)} \sum_{i<j} (\hat{\vec{R}}_i \cdot \hat{\vec{R}}_j)^2$ was introduced, where $\hat{\vec{R}}_i$ denotes the end-to-end vector (normalized to unity) of the ith polymer. By performing extensive multicanonical simulations in a parallel implementation[42] it could be shown that the bending stiffness plays a crucial role in whether the system forms an amorphous aggregate or a bundle structure.

Figure 24 shows the resulting temperature-stiffness phase diagram for eight 13mers exhibiting a regime of rather flexible polymers forming amorphous aggregates, an intermediate regime, and a regime of rather stiff polymers forming bundle-like structures. In the intermediate stiffness regime a microcanonical analysis showed that lowering the temperature first drives the system into an uncorrelated aggregate, shortly followed by a second-order-like transition into the correlated aggregate. The "frozen" (low-temperature) states in Fig. 24 show a twisted bundle structure if the stiffness is large enough. This sort of structure has been reported before in the context of material design for specific interactions usually related to proteins. Since the study of Ref. 157 did not include any specific interactions, but instead a simple coarse-grained homopolymer model with short-range attraction, hard-core repulsion and additional bending stiffness, it is tempting to conclude that specific interactions are not necessary for bundle formation. Specific interactions such as, e.g., hydrogen bonding may, however, stabilize (or destabilize) the occurring bundle structures.

4. Summary

Computer simulation studies in generalized ensembles are a powerful tool for studying the statistical physics of macromolecular systems. Focusing in these lecture notes mainly on our own recent work, this was demonstrated

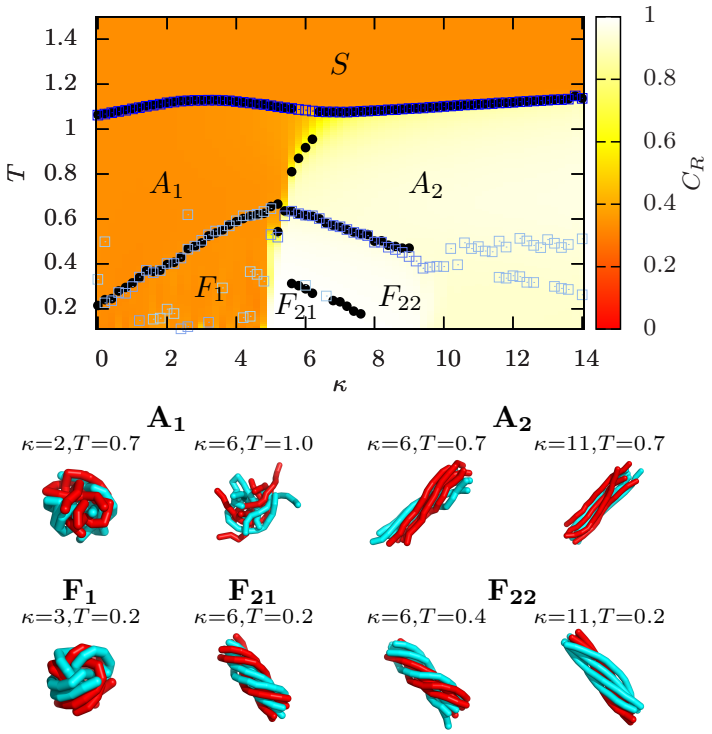

Fig. 24. Aggregation phase diagram for eight 13mers. Shown are a surface plot of the end-to-end correlation parameter C_R (see text), the maxima of the heat capacity (black dots) and the temperature derivative of the phase separation parameter Γ^2 (blue squares). Several structural phases can be distinguished: S (separated), A (aggregated), and F (frozen). In the lower panel of the figure representative conformations in the low-temperature phases are depicted (taken from Ref. 157).

with several applications of the multicanonical and the parallel tempering methods or combinations thereof to selected examples, including the physically and technologically important cases of polymer adsorption and polymer aggregation. Many similar studies have been performed with the related Wang-Landau method, which here were only briefly mentioned because of lack of space. On the computational side, it is important that multicanonical simulations can be efficiently parallelized and even allow implementations on graphics card units (GPUs), a feature that will become more and more important in future work.

Acknowledgements

First of all I wish to thank all my students, colleagues and friends who have contributed to the results presented in these lecture notes. The most important contributions emerged from collaborations with Handan Arkın, Kieran S. Austin, Michael Bachmann, Jonathan Gross, Momchil Ivanov, Christoph Junghans, Steffen Karalus, Martin Marenz, Monika Möddel, Marco Mueller, Philipp Schierz, Martin Weigel, and Johannes Zierenberg.

The work discussed here was supported by the Deutsche Forschungsgemeinschaft (DFG) through the Collaborative Research Centre SFB/TRR 102 (Project B04) and Grants Nos. JA 483/31-1 and JA 483/33-1. Further support was obtained by the Alexander von Humboldt Foundation under the Experienced Researcher Fellowship Programme, the Deutsch-Französische Hochschule (DFH-UFA) through the Doctoral College "$\mathbb{L}^4$" under Grant No. CDFA-02-07, the EU Marie Curie IRSES network DIONICOS under Contract No. PIRSES-GA-2013-612707 within the European Union Seventh Framework Programme, and the Leipzig Graduate School of Natural Sciences "BuildMoNa". The computer time for the Monte Carlo simulations was provided by NIC, Forschungszentrum Jülich, under Grant No. hlz24, which is gratefully acknowledged.

References

1. M. P. Allen and D. J. Tildesley, *Computer Simulation of Liquids*. Oxford University Press, Oxford (1987).
2. D. Frenkel and B. Smit, *Understanding Molecular Simulation: From Algorithms to Applications*, 2nd revised edition. Academic Press, New York (2001).
3. D. C. Rapaport, *The Art of Molecular Dynamics Simulations*, 2nd edition. Cambridge University Press, Cambridge (2004).
4. M. E. J. Newman and G. T. Barkema, *Monte Carlo Methods in Statistical Physics*. Clarendon Press, Oxford (1999).
5. D. P. Landau and K. Binder, *Monte Carlo Simulations in Statistical Physics*. Cambridge University Press, Cambridge (2000).
6. B. A. Berg, *Markov Chain Monte Carlo Simulations and Their Statistical Analysis*. World Scientific, Singapore (2004).
7. W. Janke, Monte Carlo simulations in statistical physics – From basic principles to advanced applications, in *Order, Disorder and Criticality: Advanced Problems of Phase Transition Theory*, Vol. 3, edited by Y. Holovatch. World Scientific, Singapore (2012), pp. 93–166.
8. B. A. Berg and T. Neuhaus, Multicanonical algorithms for first order phase transitions, *Phys. Lett.* B. **267**, 249–253 (1991).

9. B. A. Berg and T. Neuhaus, Multicanonical ensemble: A new approach to simulate first-order phase transitions, *Phys. Rev. Lett.* **68**, 9–12 (1992).
10. W. Janke, Multicanonical simulation of the two-dimensional 7-state Potts model, *Int. J. Mod. Phys.* C. **3**, 1137–1146 (1992).
11. K. Hukushima and K. Nemoto, Exchange Monte Carlo method and application to spin glass simulations, *J. Phys. Soc. Japan*. **65**, 1604–1608 (1996).
12. B. A. Berg, Introduction to multicanonical Monte Carlo simulations, *Fields Inst. Comm.* **26**, 1–24 (2000).
13. B. A. Berg, Generalized ensemble simulations for complex systems, *Comp. Phys. Comm.* **147**, 52–57 (2002).
14. B. A. Berg, A brief history of the introduction of generalized ensembles to Markov chain Monte Carlo simulations, *Eur. Phys. J. – Special Topics*. **226**, 551–565 (2017).
15. W. Janke, Multicanonical Monte Carlo simulations, *Physica* A. **254**, 164–178 (1998).
16. W. Janke, Monte Carlo methods in classical statistical physics, *Lect. Notes Phys.* **739**, 79–140 (2008).
17. U. H. E. Hansmann and Y. Okamoto, The generalized-ensemble approach for protein folding simulations, in: *Annual Reviews of Computational Physics VI*, edited by D. Stauffer. World Scientific, Singapore (1999), pp. 129–157.
18. W. Janke and W. Paul, Thermodynamics and Structure of Macromolecules from Flat-Histogram Monte Carlo Simulations, *Soft Matter*. **12**, 642–657 (2016).
19. J. Zierenberg, M. Marenz, and W. Janke, Dilute semiflexible polymers with attraction: Collapse, folding and aggregation, *Polymers*. **8**, 333-1–19 (2016).
20. F. Wang and D. P. Landau, Efficient, multiple-range random walk algorithm to calculate the density of states, *Phys. Rev. Lett.* **86**, 2050–2053 (2001).
21. F. Wang and D. P. Landau, Determining the density of states for classical statistical models: A random walk algorithm to produce a flat histogram, *Phys. Rev.* E. **64**, 056101-1–16 (2001).
22. P. N. Vorontsov-Velyaminov, N. A. Volkov, A. A. Yurchenko, and A. P. Lyubartsev, Simulation of polymers by the Monte Carlo method using the Wang-Landau algorithm, *Polym. Sci. Ser.* A. **52**, 742–760 (2010).
23. T. Wüst, Y. W. Li, and D. P. Landau, Unraveling the beautiful complexity of simple lattice model polymers and proteins using Wang-Landau sampling, *J. Stat. Phys.* **144**, 638–651 (2011).
24. S. Singh, M. Chopra, and J. J. de Pablo, Density of statesbased molecular simulations, *Annu. Rev. Chem. Biomol. Eng.* **3**, 369–394 (2012).
25. M. P. Taylor, W. Paul, and K. Binder, Applications of the Wang-Landau algorithm to phase transitions of a single polymer chain, *Polym. Sci. Ser.* C. **55**, 23–38 (2013).
26. F. Liang, A theory on flat histogram Monte Carlo algorithms, *J. Stat. Phys.* **122**, 511–529 (2006).
27. F. Liang, C. Liu, and R. J. Carroll, Stochastic approximation in Monte Carlo computation, *J. Amer. Stat. Ass.* **102**, 305–320 (2007).

28. F. Liang, On the use of stochastic approximation Monte Carlo for Monte Carlo integration, *Statist. Prob. Lett.* **79**, 581–587 (2009).
29. B. Werlich, T. Shakirov, M. P. Taylor, and W. Paul, Stochastic approximation Monte Carlo and Wang-Landau Monte Carlo applied to a continuum polymer model, *Comput. Phys. Commun.* **86**, 65–70 (2015).
30. B. Werlich, M. P. Taylor, T. Shakirov, and W. Paul, On the pseudo phase diagram of single semi-flexible polymer chains: A flat-histogram Monte Carlo study, *Polymers*. **9**, 38-1–13 (2017).
31. S. Schneider, M. Mueller, and W. Janke, Convergence of stochastic approximation Monte Carlo and modified Wang-Landau algorithms: Tests for the Ising model, *Comput. Phys. Commun.* **216**, 1–7 (2017).
32. K. Binder, Monte Carlo investigations of phase transitions and critical phenomena, in: *Phase Transitions and Critical Phenomena*, Vol. 5b, eds. C. Domb and M. S. Green. Academic Press, London (1976), pp. 1–105.
33. A. M. Ferrenberg and R. H. Swendsen, New Monte Carlo technique for studying phase transitions, *Phys. Rev. Lett.* **61**, 2635–2638 (1988) [*Phys. Rev. Lett.* **63**, 1658(E) (1989)].
34. A. M. Ferrenberg and R. H. Swendsen, Optimized Monte Carlo data analysis, *Phys. Rev. Lett.* **63**, 1195–1198 (1989).
35. S. Kumar, J. M. Rosenberg, D. Bouzida, R. H. Swendsen, and P. A. Kollman, The weighted histogram analysis method for free-energy calculations on biomolecules. I. The method, *J. Comput. Chem.* **13**, 1011–1021 (1992).
36. G. M. Torrie and J. P. Valleau, Nonphysical sampling distributions in Monte Carlo free-energy estimation – Umbrella sampling, *J. Comput. Phys.* **23**, 187–199 (1977).
37. D. Chandler, *Introduction to Modern Statistical Mechanics*. Oxford University Press, Oxford (1987), pp. 168–175.
38. U. H. E. Hansmann and Y. Okamoto, Prediction of peptide conformation by multicanonical algorithm: New approach to the multiple-minima problem, *J. Comput. Chem.* **14**, 1333–1338 (1993).
39. S. Schnabel, M. Bachmann, and W. Janke, Identification of characteristic protein folding channels in a coarse-grained hydrophobic-polar peptide model, *J. Chem. Phys.* **126**, 105102-1–6 (2007).
40. S. Schnabel, M. Bachmann, and W. Janke, Elastic Lennard-Jones polymers meet clusters – Differences and similarities, *J. Chem. Phys.* **131**, 124904-1–9 (2009).
41. S. Schnabel, W. Janke, and M. Bachmann, Advanced multicanonical Monte Carlo methods for efficient simulations of nucleation processes of polymers, *J. Comp. Phys.* **230**, 4454–4465 (2011).
42. J. Zierenberg, M. Marenz, and W. Janke, Scaling properties of a parallel implementation of the multicanonical algorithm, *Comput. Phys. Commun.* **184**, 1155–1160 (2013).
43. J. Gross, J. Zierenberg, M. Weigel, and W. Janke, Massively parallel multicanonical simulations, arXiv:1707.00919 [physics.comp-ph], submitted to Comput. Phys. Commun. (2017).
44. V. V. Slavin, Monte Carlo simulation of a two-dimensional electron gas on

a disordered host lattice, *Low Temp. Phys.* **36**, 243–249 (2010).
45. A. Ghazisaeidi, F. Vacondio, and L. A. Rusch, Filter design for SOA-assisted SS-WDM systems using parallel multicanonical Monte Carlo, *J. Lightwave Technol.* **28**, 79–90 (2010).
46. J. Zierenberg, M. Marenz, and W. Janke, Scaling properties of parallelized multicanonical simulations, *Physics Procedia*. **53**, 55–59 (2014).
47. J. Zierenberg, M. Wiedenmann, and W. Janke, Application of the parallel multicanonical method to lattice gas condensation, *J. Phys.: Conf. Ser.* **510**, 012017-1–8 (2014).
48. B. A. Berg, U. Hansmann, and T. Neuhaus, Simulation of an ensemble with varying magnetic field: A numerical determination of the order-order interface tension in the $D = 2$ Ising model, *Phys. Rev.* B. **47**, 497–500 (1993).
49. B. A. Berg, U. Hansmann, and T. Neuhaus, Properties of interfaces in the two and three dimensional Ising model, *Z. Phys.* B. **90**, 229–239 (1993).
50. B. A. Berg and W. Janke, Multi-overlap simulations of the $3d$ Edwards-Anderson Ising spin glass, *Phys. Rev. Lett.* **80**, 4771–4774 (1998).
51. B. A. Berg, A. Billoire, and W. Janke, Spin glass overlap barriers in three and four dimensions, *Phys. Rev.* B. **61**, 12143–12150 (2000).
52. H. G. Katzgraber, S. Trebst, D.A. Huse, and M. Troyer, Feedback-optimized parallel tempering Monte Carlo, *J. Stat. Mech.* P03018-1–22 (2006).
53. S. Trebst, M. Troyer, and U. H. E. Hansmann, Optimized parallel tempering simulations of proteins, *J. Chem. Phys.* **124**, 174903-1–6 (2006).
54. D. Gront and A. Kolinski, Efficient scheme for optimization of parallel tempering Monte Carlo method, *J. Phys.: Condens. Matter*. **19**, 036225-1–9 (2007).
55. E. Bittner, A. Nu ßbaumer, and W. Janke, Make life simple: Unleash the full power of the parallel tempering algorithm, *Phys. Rev. Lett.* **101**, 130603-1–4 (2008).
56. A. Milchev, A. Bhattacharaya, and K. Binder, Formation of block copolymer micelles in solution: A Monte Carlo study of chain length dependence, *Macromolecules*. **34**, 1881–1893 (2001).
57. O. Kratky and G. Porod, Röntgenuntersuchung gelöster Fadenmoleküle, *Rec. Trav. Chim. Pays-Bas.* **68**, 1106–1122 (1949).
58. P.-G. de Gennes, *Scaling Concepts in Polymer Physics*. Cornell University Press, Ithaca (1979).
59. K. S. Austin, M. Marenz, and W. Janke, Efficiencies of joint non-local update moves in Monte Carlo simulations of coarse-grained polymers, Leipzig preprint (2017), submitted to Comput. Phys. Commun.
60. T. Wüst and D. P. Landau, Optimized Wang-Landau sampling of lattice polymers: Ground state search and folding thermodynamics of HP model proteins, *J. Chem. Phys.* **137**, 064903-1–13 (2012).
61. M. Lal, Monte Carlo computer simulation of chain molecules, *Mol. Phys.* **17**, 57–64 (1969).
62. N. Madras and A. D. Sokal, Nonergodicity of local, length-conserving Monte Carlo algorithms for the self-avoiding walk, *J. Stat. Phys.* **47**, 573–595

(1987).
63. M. Bachmann, H. Arkın, and W. Janke, Multicanonical study of coarse-grained off-lattice models for folding heteropolymers, *Phys. Rev.* E. **71**, 1539–3755 (2005).
64. V. G. Mavrantza, T. D. Boone, E. Zervopoulou, and D. N. Theodorou, End-bridging Monte Carlo: A fast algorithm for atomistic simulation of condensed phases of long polymer chains, *Macromolecules*. **32**, 5072–5096 (1999).
65. K. Šolc and W. H. Stockmayer, Shape of a random-flight chain, *J. Chem. Phys.* **54**, 2756–2757 (1971).
66. K. Šolc, Shape of a random-flight chain, *J. Chem. Phys.* **55**, 335–344 (1971).
67. D. N. Theodorou and U. W. Suter, Shape of unperturbed linear polymers: Polypropylene, *Macromolecules*. **18**, 1206–1214 (1985).
68. V. Blavatska and W. Janke, Shape anisotropy of polymers in disordered environment, *J. Chem. Phys.* **133**, 184903-1–7 (2010).
69. J. Vymětal and J. Vondrášek, Gyration- and inertia-tensor-based collective coordinates for metadynamics. Application on the conformational behavior of polyalanine peptides and Trp-cage folding, *J. Phys. Chem.* A. **115**, 11455–11465 (2011).
70. V. Blavatska and W. Janke, Polymer adsorption on a fractal substrate: Numerical study, *J. Chem. Phys.* **136**, 104907-1–8 (2012).
71. B. Efron, *The Jackknife, the Bootstrap and Other Resampling Plans*. Society for Industrial and Applied Mathematics [SIAM], Philadelphia (1982).
72. W. Janke, *Monte Carlo methods in classical statistical physics*, in: *Computational Many-Particle Physics*, Wilhelm & Else Heraeus Summerschool, Greifswald, edited by H. Fehske, R. Schneider, and A. Weiße, Lect. Notes Phys. **739**. Springer, Berlin, (2008), pp. 79–140.
73. P. N. Vorontsov-Velyaminov, N. A. Volkov, and A. A. Yurchenko, Entropic sampling of simple polymer models within WangLandau algorithm, *J. Phys.* A: Math. Gen. **37**, 1573–1588 (2004).
74. N. A. Volkov, A. A. Yurchenko, A. P. Lyubartsev, and P. N. Vorontsov-Velyaminov, Entropic sampling of free and ring polymer chains, *Macrom. Theory Simul.* **14**, 491–504 (2005).
75. F. Rampf, W. Paul, and K. Binder, On the first-order collapse transition of a three-dimensional, flexible homopolymer chain model, *Europhys. Lett.* **70**, 628–634 (2005).
76. F. Rampf, K. Binder, and W. Paul, The phase diagram of a single polymer chain: New insights from a new simulation method, *J. Pol. Sci.* B: Pol. Phys. **44**, 2542–2555 (2006).
77. M. P. Taylor, W. Paul, and K. Binder, Phase transitions of a single polymer chain: A Wang-Landau simulation study, *J. Chem. Phys.* **131**, 114907-1–9 (2009).
78. M. P. Taylor, W. Paul, and K. Binder, All-or-none proteinlike folding transition of a flexible homopolymer chain, *Phys. Rev.* E. **79**, 050801(R)-1–4 (2009).
79. J. Gross, T. Neuhaus, T. Vogel, and M. Bachmann, Effects of the interaction

range on structural phases of flexible polymers. *J. Chem. Phys.* **138**, 074905-1–8 (2013).
80. T. Koci and M. Bachmann, Confinement effects upon the separation of structural transitions in linear systems with restricted bond fluctuation ranges, *Phys. Rev.* E. **92**, 042142-1–9 (2015).
81. W. Paul, T. Strauch, F. Rampf, and K. Binder, Unexpectedly normal phase behavior of single homopolymer chains, *Phys. Rev.* E. **75**, 060801(R)-1–4 (2007).
82. T. Vogel, M. Bachmann, and W. Janke, Freezing and collapse of flexible polymers on regular lattices in three dimensions, *Phys. Rev.* E. **76**, 061803-1–11 (2007).
83. D. F. Parsons and D. R. Williams, Globule transitions of a single homopolymer: A Wang-Landau Monte Carlo study, *Phys. Rev.* E. **74**, 041804-1–10 (2006).
84. D. F. Parsons and D. R. Williams, An off-lattice Wang-Landau study of the coil-globule and melting transitions of a flexible homopolymer, *J. Chem. Phys.* **124**, 221103-1–4 (2006).
85. D. Seaton, T. Wüst, and D. P. Landau, Collapse transitions in a flexible homopolymer chain: Application of the Wang-Landau algorithm, *Phys. Rev.* E. **81**, 011802-1–10 (2010).
86. S. Majumder, J. Zierenberg, and W. Janke, Kinetics of polymer collapse: Effect of temperature on cluster growth and aging, *Soft Matter*. **13**, 1276–1290 (2017).
87. M. J. Stephen, Collapse of a polymer chain, *Phys. Lett.* **53A**, 363–364 (1975).
88. B. Duplantier, Lagrangian tricritical theory of polymer chain solutions near the θ-point, *J. Phys. France* **43**, 991–1019 (1982).
89. A. L. Kholodenko and K. F. Freed, Theta point ("tricritical") region behavior for a polymer chain: Transition to collapse, *J. Chem. Phys.* **80**, 900–924 (1984).
90. B. Duplantier, Tricritical polymer chains in or below three dimensions, *Europhys. Lett.* **1**, 491–498 (1986).
91. B. Duplantier, Geometry of polymer chains near the theta-point and dimensional regularization, *J. Chem. Phys.* **86**, 4233–4244 (1987).
92. P. Grassberger and R. Hegger, Simulations of three-dimensional θ polymers, *J. Chem. Phys.* **102**, 6881–6899 (1995).
93. J. Hager and L. Schäfer, θ-point behavior of diluted polymer solutions: Can one observe the universal logarithmic corrections predicted by field theory? *Phys. Rev.* E. **60**, 2071–2085 (1999).
94. D. T. Seaton, S. Schnabel, D. P. Landau, and M. Bachmann, From flexible to stiff: Systematic analysis of structural phases for single semiflexible polymers, *Phys. Rev. Lett.* **110**, 028103-1–5 (2013).
95. M. Marenz and W. Janke, Effect of bending stiffness on a generic polymer and where knots come into play, *Phys. Rev. Lett.* **116**, 128301-1–6 (2016).
96. E. Bittner and W. Janke, Free-energy barriers in the Sherrington-Kirkpatrick model, *Europhys. Lett.* **74**, 195–201 (2006).

97. M. Marenz and W. Janke, Effect of bending stiffness on a homopolymer inside a spherical cage, *Physics Procedia*. **57**, 53–57 (2014).
98. W. Janke and M. Marenz, Stable knots in the phase diagram of semiflexible polymers: A topological order parameter? *J. Phys.: Conf. Ser.* **750**, 012006-1–5 (2016).
99. W. Janke and M. Marenz, preprint in preparation (2017).
100. D. T. Seaton, S. Schnabel, M. Bachmann, and D. P. Landau, Effects of stiffness on short, semiflexible homopolymer chains, *Int. J. Mod. Phys.* C. **23**, 1240004-1–7 (2012).
101. D. Reith, P. Cifra, A. Stasiak, and P. Virnau, Stiffening of DNA due to nematic ordering causes DNA molecules packed in phage capsids to preferentially form torus knots, *Nucleic Acids Res.* **40**, 5129–5137 (2012).
102. P. Virnau, Detection and visualization of physical knots in macromolecules, *Physics Procedia*. **6**, 117–125 (2010).
103. L. H. Kauffman, *Knots and Physics*, 2nd edition. World Scientific, Singapore (1991).
104. W. Janke, Accurate first-order transition points from finite-size data without power-law corrections, *Phys. Rev.* B. **47**, 14757–14770 (1993).
105. W. Janke, First-order phase transitions, in: *Computer Simulations of Surfaces and Interfaces*, NATO Science Series, II. Mathematics, Physics and Chemistry – Vol. **114**, edited by B. Dünweg, D. P. Landau and A. I. Milchev. Kluwer, Dordrecht (2003), pp. 111–135.
106. Y. Yoshida and Y. Hiwatari, Properties of a simple polymer chain in a narrow capillary - 2 dimensional Monte Carlo study, *Mol. Simul.* **22**, 91–121 (1999).
107. M. Bachmann and W. Janke, Conformational transitions of non-grafted polymers near an adsorbing substrate, *Phys. Rev. Lett.* **95**, 058102-1–4 (2005).
108. M. Möddel, M. Bachmann, and W. Janke, Conformational mechanics of polymer adsorption transitions at attractive substrates, *J. Phys. Chem.* B. **113**, 3314–3323 (2009).
109. M. Möddel, W. Janke, and M. Bachmann, Systematic microcanonical analyses of polymer adsorption transitions, *Phys. Chem. Chem. Phys.* **12**, 11548–11554 (2010).
110. M. Möddel, W. Janke, and M. Bachmann, Adsorption of finite polymers in different thermodynamical ensembles, *Comput. Phys. Commun.* **182**, 1961–1965 (2011).
111. T. Chen, L. Wang, X. Liu, and H. Liang, Microcanonical analysis of adsorption of homopolymer chain on a surface, *J. Chem. Phys.* **130**, 244905-1–6 (2009).
112. N. A. Volkov, P. N. Vorontsov-Velyaminov, and A. P. Lyubartsev, Two-dimensional Wang-Landau algorithm for osmotic pressure calculations in a polyelectrolyte-membrane system, *Macromol. Theory Simul.* **20**, 496–509 (2011).
113. J. Luettmer-Strathmann, F. Rampf, W. Paul, and K. Binder, Transitions of tethered polymer chains, *J. Chem. Phys.* **128**, 064903-1–15 (2008).

114. J. Luettmer-Strathmann and K. Binder, Transitions of tethered chain molecules under tension, *J. Chem. Phys.* **141**, 114911-1–18 (2014).
115. M. P. Taylor and J. Luettmer-Strathmann, Partition function zeros and finite size scaling for polymer adsorption, *J. Chem. Phys.* **141**, 204906-1–10 (2014).
116. V. A. Ivanov, J. A. Martemyanova, M. Müller, W. Paul, and K. Binder, Conformational changes of a single semiflexible macromolecule near an adsorbing surface: A Monte Carlo simulation, *J. Phys. Chem.* B. **113**, 3653–3668 (2009).
117. W. A. Steele, The physical interaction of gases with crystalline solids. I. Gas-solid energies and properties of isolated adsorbed atoms, *Surf. Sci.* **36**, 317–352 (1973).
118. M. Möddel, W. Janke, and M. Bachmann, Comparison of the adsorption transition for grafted and non-grafted polymers, *Macromolecules*. **44**, 9013–9019 (2011).
119. T. Chen, L. Wang, X. Lin, Y. Liu, and H. Liang, Microcanonical analysis of adsorption of homopolymer chain on a surface, *J. Chem. Phys.* **130**, 244905-1–6 (2009).
120. L. Wang, T. Chen, X. Lin, Y. Liu, and H. Liang, Canonical and microcanonical analysis of nongrafted homopolymer adsorption by an attractive substrate, *J. Chem. Phys.* **131**, 244902-1–8 (2009).
121. H. Arkın and W. Janke, Structural behavior of a polymer chain inside an attractive sphere, *Phys. Rev.* E. **85**, 051802-1–9 (2012).
122. H. Arkın and W. Janke, Ground-state properties of a polymer chain in an attractive sphere, *J. Phys. Chem.* B. **116**, 10379–10386 (2012).
123. H. Arkın and W. Janke, Gyration tensor based analysis of the shapes of polymer chains in an attractive spherical cage, *J. Chem. Phys.* **138**, 054904-1–8 (2013).
124. H. Arkın and W. Janke, Polymer–attractive spherical cage system, *Eur. Phys. J. – Special Topics*. **216**, 181–190 (2013).
125. M. Möddel, W. Janke, and M. Bachmann, Adsorption and pattern recognition of polymers at complex surfaces with attractive stripe-like motifs, *Phys. Rev. Lett.* **112**, 148303-1–5 (2014).
126. S. Karalus, W. Janke, and M. Bachmann, Thermodynamics of polymer adsorption to a flexible membrane, *Phys. Rev.* E. **84**, 031803-1–12 (2011).
127. K.S. Austin, J. Zierenberg, and W. Janke, Interplay of adsorption and semiflexibility: Structural behavior of grafted polymers under poor solvent conditions, *Macromolecules*. **50**, 4054–4063 (2017).
128. M. Campoy-Quiles, T. Ferenczi, T. Agostinelli, P. G. Etchegoin, Y. Kim, T. D. Anthopoulos, P. N. Stavrinou, D. D. C. Bradley, and J. Nelson, Morphology evolution via self-organization and lateral and vertical diffusion in polymer: Fullerene solar cell blends, *Nat. Mater.* **7**, 158–164 (2008).
129. F. Chiti and C. M. Dobson, Protein misfolding, functional amyloid, and human disease, *Annu. Rev. Biochem.* **75**, 333–366 (2006).
130. S. Förster, E. Kohl, M. Ivanov, J. Gross, W. Widdra, and W. Janke, Polymer adsorption on reconstructed Au(001): A statistical description of P3HT

by scanning tunneling microscopy and coarse-grained Monte Carlo simulations, *J. Chem. Phys.* **141**, 164701-1–8 (2014).
131. K. Goede, P. Busch, and M. Grundmann, Binding specificity of a peptide on semiconductor surfaces, *Nano Lett.* **4**, 2115–2120 (2004).
132. D. H. E. Gross, *Microcanonical Thermodynamics*. World Scientific, Singapore (2001).
133. R. Hammer, A. Höfer, S. Förster, M. Kiel, K. Meinel, and W. Widdra, Surface reconstruction of Au(001): High-resolution real-space and reciprocal-space inspection, *Phys. Rev.* B. **90**, 035446-1–13 (2014).
134. H. Heinz, R. A. Vaia, B. L. Farmer, and R. R. Naik, Accurate simulation of surfaces and interfaces of face-centered cubic metals using 12–6 and 9–6 Lennard-Jones potentials, *J. Phys. Chem.* C. **112**, 17281–17290 (2008).
135. R. Hentschke, Molecular modeling of adsorption and ordering at solid interfaces, *Macromol. Theory Simul.* **6**, 287–316 (1997).
136. D. M. Huang, R. Faller, K. Do, and A. J. Moule, Coarse-grained computer simulations of polymer/fullerene bulk heterojunctions for organic photovoltaic applications, *J. Chem. Theory Comput.* **6**, 526–537 (2010).
137. M. Waldman and A. T. Hagler, New combining rules for rare gas van der Waals parameters, *J. Comp. Chem.* **14**, 1077–1084 (1993).
138. C. Junghans, M. Bachmann, and W. Janke, Microcanonical analyses of peptide aggregation processes, *Phys. Rev. Lett.* **97**, 218103-1–4 (2006).
139. C. Junghans, M. Bachmann, and W. Janke, Thermodynamics of peptide aggregation processes: An analysis from perspectives of three statistical ensembles, *J. Chem. Phys.* **128**, 085103-1–9 (2008).
140. M. Bachmann, H. Arkın, and W. Janke, Multicanonical study of coarse-grained off-lattice models for folding heteropolymers, *Phys. Rev.* E. **71**, 031906-1–11 (2005).
141. W. Janke, Canonical versus microcanonical analysis of first-order phase transitions, *Nucl. Phys.* B (Proc. Suppl.). **63A-C**, 631–633 (1998).
142. C. Junghans, W. Janke, and M. Bachmann, Hierarchies in nucleation transitions, *Comput. Phys. Commun.* **182**, 1937–1940 (2011).
143. T. Chen, X. Lin, Y. Liu, and H. Liang, Microcanonical analysis of association of hydrophobic segments in a heteropolymer, *Phys. Rev.* E. **76**, 046110-1–4 (2007).
144. R. B. Frigori, L. G. Rizzi, and N. A. Alves, Microcanonical thermostatistics of coarse-grained proteins with amyloidogenic propensity, *J. Chem. Phys.* **138**, 015102-1–7 (2013).
145. C. Junghans, M. Bachmann, and W. Janke, Statistical mechanics of aggregation and crystallization for semiflexible polymers, *Europhys. Lett.* **87**, 40002-1–5 (2009).
146. T. Chen, X. Lin, Y. Liu, T. Lu, and H. Liang, Microcanonical analyses of homopolymer aggregation processes, *Phys. Rev.* E. **78**, 056101-1–5 (2008).
147. J. Zierenberg, M. Mueller, P. Schierz, M. Marenz, and W. Janke, Aggregation of theta-polymers in spherical confinement, *J. Chem. Phys.* **141**, 114908-1–9 (2014).
148. A. Nußbaumer, E. Bittner, and W. Janke, Monte Carlo study of the droplet

formation-dissolution transition on different two-dimensional lattices, *Phys. Rev.* E. **77**, 041109-1–11 (2008).
149. J. Zierenberg and W. Janke, Exploring different regimes in finite-size scaling of the droplet condensation-evaporation transition, *Phys. Rev.* E. **92**, 012134-1–11 (2015).
150. K. Binder and M. H. Kalos, Critical clusters in a supersaturated vapor: theory and Monte Carlo simulation, *J. Stat. Phys.* **22**, 363-396 (1980).
151. H. Furukawa and K. Binder, Two-phase equilibria and nucleation barriers near a critical point, *Phys. Rev.* A. **26**, 556-566 (1982).
152. M. Biskup, L. Chayes, and R, Kotecký, On the formation/dissolution of equilibrium droplets, *Europhys. Lett.* **60**, 21-27 (2002).
153. M. Biskup, L. Chayes, and R. Kotecký, Critical region for droplet formation in the two-dimensional Ising model, *Commun. Math. Phys.* **242**, 137-183 (2003).
154. T. Neuhaus and J. Hager, 2D crystal shapes, droplet condensation, and exponential slowing down in simulations of first-order phase transitions, *J. Stat. Phys.* **113**, 47-83 (2003).
155. K. Binder, Theory of the evaporation/condensation transition of equilibrium droplets in finite volumes. *Physica* A. **319**, 99-114 (2003).
156. J. Zierenberg, P. Schierz, and W. Janke, Canonical free-energy barrier of particle and polymer cluster formation, *Nat. Commun.* **8**, 14546-1–7 (2017).
157. J. Zierenberg and W. Janke, From amorphous aggregates to polymer bundles: The role of stiffness on structural phases in polymer aggregation, *Europhys. Lett.* **109**, 28002-1–6 (2015).